NANO LETTERS

Letter

pubs.acs.org/NanoLett

Temperature-Gated Thermal Rectifier for Active Heat Flow Control

Jia Zhu,[†,∥] Kedar Hippalgaonkar,[†,∥] Sheng Shen,[†] Kevin Wang,[‡] Yohannes Abate,[§] Sangwook Lee,[‡] Junqiao Wu,[‡] Xiaobo Yin,[†] Arun Majumdar,*[,†] and Xiang Zhang*[,†]

[†]Department of Mechanical Engineering and [‡]Department of Materials Science and Engineering, University of California at Berkeley, Berkeley, California 94720, United States

[§]Department of Physics and Astronomy, Georgia State University, Atlanta, Georgia 30303, United States

Supporting Information

ABSTRACT: Active heat flow control is essential for broad applications of heating, cooling, and energy conversion. Like electronic devices developed for the control of electric power, it is very desirable to develop advanced all-thermal solid-state devices that actively control heat flow without consuming other forms of energy. Here we demonstrate temperature-gated thermal rectification using vanadium dioxide beams in which the environmental temperature actively modulates asymmetric heat flow. In this three terminal device, there are two switchable states, which can be regulated by global heating. In the "Rectifier" state, we observe up to 28% thermal rectification. In the "Resistor" state, the thermal rectification is significantly suppressed (<1%). To the best of our knowledge, this is the first demonstration of solid-state active-thermal devices with a large rectification in the Rectifier state. This temperature-gated rectifier can have substantial implications ranging from autonomous thermal management of heating and cooling systems to efficient thermal energy conversion and storage.

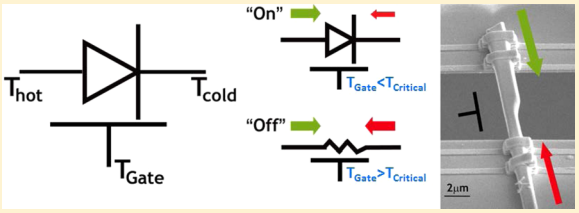

KEYWORDS: *Thermal rectification, nanoscale heat transport, vanadium dioxide, phonons*

Heat and charge transport in condensed matter were first characterized about two centuries ago by the well-known Fourier's[1] ($\vec{q} = -k\nabla\vec{T}$) and Ohm's[2] ($\vec{J} = -\sigma\vec{E}$) laws, respectively. The history of how the science of heat and charge transport has evolved, however, is very different. The progress in material processing (such as purification of semiconductors) and fundamental understanding (quantum mechanics) led to the invention of many electronic devices such as transistors to actively control and manipulate charge transport. Such devices have been widely deployed and have touched almost all aspects of modern life in what we now call the information revolution. In stark contrast, heat transport in condensed matter has remained in the realm of the Fourier law and its manipulation beyond has been largely absent. Yet, about 90% of the world's energy utilization occurs through heating and cooling, making it one of the most critical aspects of any modern economy.[3] Hence, the ability to actively manipulate heat transport in ways akin to that for charge transport could potentially significantly impact utilization of energy resources.

A few theoretical proposals have been made envisioning control of heat flow in solid-state devices[4,5] and electrically tuned solid-state thermal memory has recently been experimentally realized.[6] Most development has explored the possibility of thermal rectification[7,8] in which the system thermal conductance depends on the direction of thermal gradient. The level of thermal rectification is commonly[7] defined as the following

$$R = \frac{G_H - G_L}{G_L}$$

Here G_H and G_L are the thermal conductances of the sample in the directions of higher and lower heat flows under the same temperature difference, respectively. Several approaches have been theorized for achieving thermal rectification, such as using materials with opposite trends in thermal conductivity as a function of temperature[9,10] or asymmetrical phonon density of states in graphene nanoribbons.[11] The rapid advancement of nanofabrication has enabled the synthesis of nanostructures with a variety of materials for both novel applications[12−16] and to explore condensed matter science.[17] Specifically, individual carbon or boron nitride nanotubes with asymmetric mass loading were reported to have thermal rectification of about 2−7%.[7] However, a pure active thermal device where heat as an input can modulate thermal transport has never been realized.

In condensed matter, both phonons and electrons carry heat. Metals are generally good conductors of heat through electrons. Manipulating heat in nonmetals requires tuning of quantized lattice vibrations or phonons. Heat transfer with a single energy carrier (either electrons and phonons) has been studied in detail in many condensed matter systems. Can the interplay between the two energy carriers at metal−insulator interfaces potentially lead to an asymmetry when the direction of heat flow is reversed? Very early work in a CuO−Cu system showed

Received: June 17, 2014
Published: July 10, 2014

   dx.doi.org/10.1021/nl502261m | *Nano Lett.* 2014, 14, 4867−4872

thermal rectification due to a single metal−insulator interface.[18] Here we demonstrate the first temperature-gated thermal rectifier devices using VO_2 beams. Interestingly, thermal rectification in the beams can be actively switched on and off by changing the device temperature, which controls the metallic and insulating phases, thus functioning as a thermal gate. Maximum rectification of 28% is observed below 340 K when mixed metallic and insulating phases coexist in the VO_2 beam. Once the devices are heated above 340 K and they become completely metallic, they behave as ordinary thermal resistors, where thermal rectification is switched off (<1%) (see Figure 1A for a depiction of the device functionality).

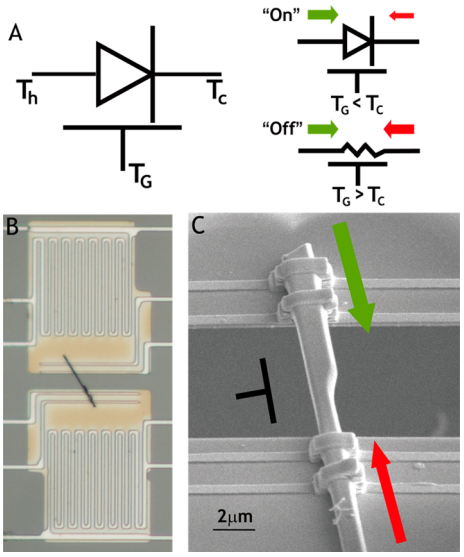

Figure 1. (A) Symbolic diagram of temperature-gated thermal rectifier. In the "Rectification" or "on" state, thermal flow depends on the direction of applied thermal gradient, representing thermal rectification. In the "Resistor" or "off" state, thermal flow does not depend on the sign of thermal gradient, essentially the behavior of a resistor. The on/off state can be controlled by T_G. (B) Optical microscope image of an asymmetrical VO_2 beam on suspended membranes for thermal conductance measurement. (C) Scanning electron microscopy (SEM) image of an asymmetrical VO_2 beam. The VO_2 beams used in this study have a uniform thickness (typically 500 nm to 1 μm) with one end of narrow width (300−900 nm) and the other end of wide width (600 nm to 2 μm). The heat flow through the beam (Q) in either direction denoted by the arrows is accurately measured while the suspended platforms are maintained as isotherms at hot and cold temperatures, T_h and T_c, respectively (details in Supporting Information).

Our material system of choice for this study is the family of vanadium oxides. Single crystalline VO_2 beams have been investigated extensively as a unique material system for studying the complexity of metallic and insulating phases that can be induced by temperature, strain, stoichiometry and light.[19−23] Thin films of polycrystalline VO_2 have shown that the insulator-to-metal transition occurs at the transition temperature ~340 K via nucleation of isolated nanoscale puddles of metallic phases in a background of the insulator phase, which then grow and merge as the transition progresses.[24] The thermal conductivity of polycrystalline stoichiometric VO_2 films was also studied close to ~340 K and increased by as much as 60% due to the phase transition.[25]

We synthesized VO_2 beams using a modified vapor transport method (Supporting Information Methods) and studied their electrical properties.[26] The structure and electrical properties confirm a VO_2 backbone. From the synthesized beams, we specifically selected beams that are tapered in shape (similar to the beam illustrated in Figure 1B,C), expecting local stresses and stoichiometry changes that could enable the coexistence of metallic and insulating phases coexisting in the beam.[19] Such a 5−10 μm long tapered beam is then transferred to a silicon microdevice so as to form a bridge between two parallel, suspended SiN_X membranes, each consisting of microfabricated symmetric resistive platinum coils, for thermal and electrical transport measurements[27] (Figure 1B). The platinum coils are used as both heaters and resistive thermometers (Supporting Information Methods). To make electrical and thermal contact, a platinum/carbon composite was deposited symmetrically on both ends using a focused ion beam. Therefore, both thermal and electrical conductance can be measured for the device. A resistive heater is used to heat the whole chip uniformly inside a cryostat to control the global device temperature, T_G. The measurement is performed in a cryostat at ~2 μTorr to prevent conduction and convection losses. (Supporting Information 2).

Figure 2A shows measured heat flow, Q, and the temperature difference, ΔT, across a tapered beam at T_G =320 K below the VO_2 insulator−metal phase transition temperature of 340 K. The heat flow, Q, increases linearly with ΔT (<1 K). However, the thermal conductance, $G = Q/\Delta T$, or the slope, differs depending on the direction of heat flow. The thermal conductance of the tapered beam when heat is flowing from the narrow to the broader side (62.2 ± 0.5 nW/K) is significantly smaller than that in the other direction (80.1 ± 0.6 nW/K). This represents a 28 ± 1.4% thermal rectification, which is the highest ever reported to the best of our knowledge. Also shown in Figure 2B is δQ, which is the deviation of the heat flow in one direction, Q, from the extrapolated linear curve representing the conductance in the opposite direction. Figure 2C,D shows similar plots for the same VO_2 beam at T_G = 385 K, which is higher than the phase transition temperature where the VO_2 beam is fully metallic. In contrast to Figure 2A,B, it is clear that no rectification is observed and the thermal conductance in both directions increases to 94 ± 0.4 nW/K. The same plots of Q and δQ at 320 K of a uniform or untapered VO_2 beam show that there is no rectification (Supporting Information 3a).

The maximum thermal rectification of six tapered VO_2 beams are tabulated in Table 1 for T_G < 340 K. The values range from 10 to 20% for different beams and T_G is different for different beams. Rectification is turned off to below 1% for T_G > 340 K. Note that in beam V, the rectification persists above the insulator-to-metal transition for stoichiometric VO_2. We ascribe this to an excess of oxygen, thus shifting the electronic transition temperature to much higher temperatures. As control experiments, symmetric beams with uniform width, which have no variation in stoichiometry, are also measured and no apparent thermal rectification effects are observed (<3%) at all temperatures below and above the transition temperature of 340 K (Supporting Information 3b).

Figure 3A shows the thermal conductance in the two directions (green and red) as a function of global temperature for a representative VO_2 beam. Between 250 and 340 K, the conductance is different in different directions, which is discussed in detail later. It is observed that the degree of rectification, R, (black closed circles) peaks at 320 K, lower than

dx.doi.org/10.1021/nl502261m | Nano Lett. 2014, 14, 4867−4872

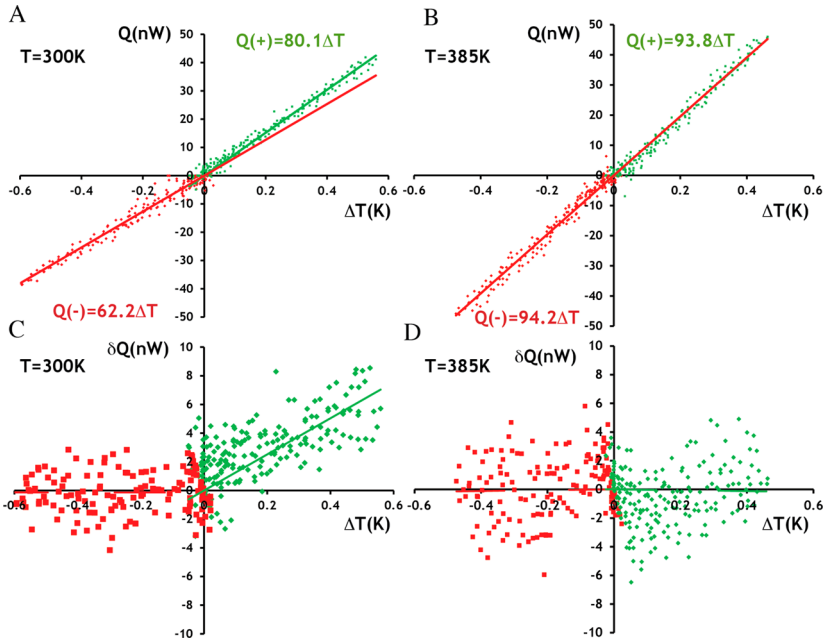

Figure 2. (A,C) Q as a function of ΔT across the VO_2 beams at 300 and 350 K, respectively. Different signs (+) and (−) of Q represent different directions of heat transfer. (B,D) Heat flow deviation (δQ) as a function of temperature difference across the VO_2 beams at 300 and 385 K, respectively.

Table 1. Thermal Conductance and Maximum Thermal Rectification (at T_G = 300−320 K) of six Different VO_2 Beams

	T_G < 340 K			T_G > 340 K		
no.	G+ (nW/K)	G− (nW/K)	R (%)	G+ (nW/K)	G− (nW/K)	R (%)
I	80.1 ± 0.6	62.2 ± 0.5	28.8 ± 1.4%	93.8 ± 0.4	94.2 ± 0.4	−0.5 ± 0.6%
II	144 ± 2.1	123 ± 1.6	16.9 ± 2.0%	165 ± 2.7	167 ± 3.0	1.0 ± 2.4%
III	113 ± 0.3	103 ± 0.3	9.1 ± 0.4%	119 ± 0.4	117 ± 0.3	1.1 ± 0.4%
IV	191 ± 0.8	171 ± 0.6	12.1 ± 0.6%	181 ± 0.6	181 ± 0.6	0.0 ± 0.5%
V	58.5 ± 0.1	55.3 ± 0.1	5.9 ± 0.2	58.6 ± 0.1	56.8 ± 0.1	3.2 ± 0.2
VI	181 ± 0.5	169 ± 0.6	7.2 ± 0.5%	186 ± 0.5	184 ± 0.6	0.9 ± 0.5%

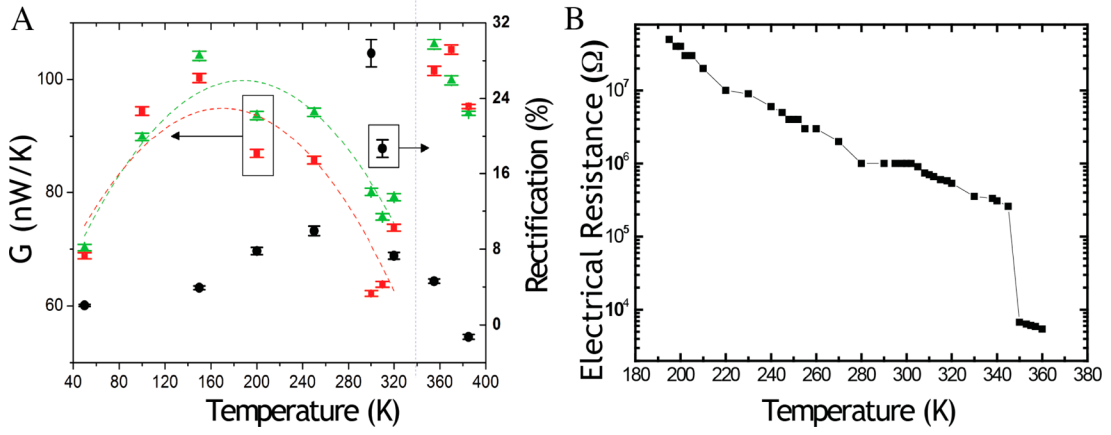

Figure 3. (A) Thermal conductance of an asymmetrical VO_2 beam as a function of global temperatures along two opposite directions (green triangles and red squares). The thermal conductance is found to be measurably higher when heat flows from the wide end to the narrow end. At low temperatures, the rectification (black closed circles) disappears and the conductance from either end is identical; this is expected as the whole wire is in the insulating phase and should behave as a normal dielectric. (B) The electrical resistance of VO_2 beam as a function of global temperature. The resistance could not be measured below 180 K due to saturation. The arrows in Figure 1 denote the direction of heat flow in which high (green) and low (red) thermal conductance was observed.

the phase transition of 340 K and decreases as the temperature is increased or decreased away from the transition. Above the VO_2 insulator−metal transition temperature (~340 K), the electronic density of states at the Fermi level increase significantly and electrons start contributing to the thermal conductance, which explains a sudden increase. This is also consistent with electrical resistance measurements (see Figure 3B), which show a drop in magnitude by two orders at 340 K

dx.doi.org/10.1021/nl502261m | *Nano Lett.* 2014, 14, 4867−4872

indicating the characteristic insulator-to-metal phase transition, consistent with reports in literature for the electronic VO_2 phase transition.[22] Below 135 K, the electronic contribution is negligible and phonons dominate heat conduction. In this temperature range, we do not observe any rectification as well. The phonon mean free path is limited by scattering from either defects, interfaces, or boundaries, and the thermal conductance increases with temperature due to increase in phonon population. Temperature-dependent conductance and rectification plots similar to Figure 3A for beam II are shown in Supporting Information 4.

In order to understand the mechanism behind temperature-dependent rectification, we first consider the effect of the asymmetric geometry on the phonon mean free path. It has been proposed that an asymmetric geometry or roughness may cause thermal rectification in materials when phonons dominate heat conduction and the phonon mean free path is comparable to the characteristic length of the structure.[4] The average phonon mean free path can be estimated by kinetic theory: $\Lambda = (3k)/(cv_g)$. In the insulating phase at 300 K, $k \approx 6$ Wm^{-1} K^{-1} is the measured thermal conductivity of a representative VO_2 beam, the volumetric heat capacity $c = 3$ J cm^{-3} K^{-1} is taken to be the bulk value of VO_2,[28] and $v_g \approx v_s \approx 4000$ ms^{-1} is estimated from the acoustic speed of sound in the c-axis [001] direction,[29] thus $\Lambda \approx 1.5$ nm. In the metallic phase at 350 K, if we take $k \approx 6$ Wm^{-1} K^{-1}, $c = 3$ J cm^{-3} K^{-1} and $v_s \approx 4000$ ms^{-1}, then $\Lambda \approx 1.5$ nm. Note that our estimation of the phonon mean free path based on kinetic theory is an underestimation since (a) the average phonon group velocity is smaller than the speed of sound, which arises from the acoustic modes. Especially accounting for multiple atoms in the primitive cell of VO_2, the optical modes can contribute significantly to the thermal conductivity, and (b) phonon scattering is highly frequency dependent, and here we estimate using only the gray model, which ascribes a frequency-independent mean free path. However, considering that the lateral length scale of our beams is ~1000 times higher than the estimated mean free path, thermal rectification due to a geometric effect that requires boundary scattering to be dominant is very unlikely. In addition, below 50 K the phonon mean free path should increase by about 1 order of magnitude. Therefore, any thermal rectification caused by asymmetrical geometry should be a lot more significant at lower temperature, which is not observed in Figure 3A. So it is not possible that uneven phonon heat conduction due to asymmetrical geometry could cause the observed large thermal rectification. This further indicates that the macroscopic geometric ratio between the broad and narrow widths of the beam across the taper is not expected to scale with the observed thermal rectification.

Next, we explore if the insulator-to-metal phase transition in VO_2 can be responsible for thermal rectification. A recent theoretical study estimated the thermal interface resistance (TIR) on the metallic side between a metal and an insulator by employing the two-temperature model to account for the lack of equilibrium between electrons and phonons near a metal−insulator interface.[30] This model only considers the TIR due to the electron−phonon cooling rate, G_{e-l}. The phonon−electron cooling rate, G_{l-e} can be different, leading to an asymmetry close to the interface. This forms the basis for the theoretical prediction of thermal rectification if metallic and insulating phases coexist in a material system.[8] Further, due to nonlinearity and asymmetry in the electron−phonon interaction another prediction estimates rectification in a one-dimensional chain that depends on the coupling strength and the temperature gradient across the interface.[31] Thus, in order to observe significant thermal rectification in a metal−insulator system, first the thermal resistance due to electron−phonon scattering should dominate over the phonon−phonon coupling resistance. In the vanadium oxide system, a small ~1% lattice distortion[22] in the rutile and monoclinic phases should ensure good acoustic match to reduce thermal resistance from phonon−phonon coupling. Therefore, it is possible that the electron−phonon scattering may be dominant for the thermal resistance at metal−insulator interfaces in VO_2 beams. Second, an abundance of coexisting metallic and insulating phases with an inherent asymmetry must prevail in the beams. Previous work has shown the coexistence of metallic and insulating phases within a single beam during phase transition.[19,20,22]

Intriguingly, in our case thermal rectification was observed not only near phase transition temperature 340 K but also over large span of temperature ~100 K below, provoking the question as to the role of the taper of the VO_2 beams. Even though the VO_2 beams show characteristic electronic transition temperature (340 K) (Supporting Information 5), it has been known that vanadium oxide can form Magnéli phases with a deficiency of oxygen, given by the general formula V_nO_{2n-1}, or excess of oxygen described by V_nO_{2n+1}. These are crystallographic shear compounds with a rutile VO_2 backbone.[32] The role of stoichiometry in $V_nO_{2n-1} = V_2O_3 + (n-2)VO_2$, or $V_nO_{2n+1} = V_2O_5 + (n-2)VO_2$ single crystals has been studied in meticulous detail.[33] As observed in Figure 3A, the "on" state of rectification exists between 250 and 340 K, where the V_2O_3/V_2O_5 shear planes would be metallic and the VO_2 matrix would be insulating. Therefore, a small variation in stoichiometry of vanadium oxide can cause the existence of metal−insulator interfaces over a very large range of temperature.[33] This is suggested in Figure 3A, between 250 and 340 K where rectification exists, in the regime where thermal conductance decreases with increasing temperature. While phonon−phonon Umklapp scattering is one possible cause for this behavior, it can also be attributed to the appearance of interfaces created by the formation and coexistence of multiple phases of vanadium oxide that may be not electronically connected, nevertheless impeding phonons due to interface scattering.

The second critical requirement to observe rectification is an asymmetry in these mixed states. In order to directly image the mixed phases and their spatial organization, we employed a scattering type scanning near-field optical microscope (s-SNOM). s-SNOM allows direct imaging of the evolution of insulating and metallic phases with increasing temperature with high spatial resolution as demonstrated previously for micro-crystals and polycrystalline films. A linearly polarized probing CO_2 laser (wavelength, $\lambda = 10.7$ μm) is focused on the tip−sample interface. High harmonic demodulation coupled with pseudoheterodyne interferometer are used to detect the near-field signal with ~30 nm spatial resolution above the tapered VO_2 beam.[24,34] The image contrast is determined by the local spatially varying dielectric function of the surface. Hence, regions of the metallic phase due to larger effective tip−sample polarizablility result in higher s-SNOM amplitude signal compared with that of the insulating phase (more details about the technique are discussed in Supporting Information 6). The wavelength of the laser was chosen specifically in order to maximize the difference in the optical conductivity of the insulating and metallic phases of VO_2 and thus achieve optimum s-SNOM amplitude contrast at different temper-

dx.doi.org/10.1021/nl502261m | Nano Lett. 2014, 14, 4867−4872

atures. Interestingly, for a tapered beam (AFM topography shown in Figure 4A,D) demonstrating ~15% thermal

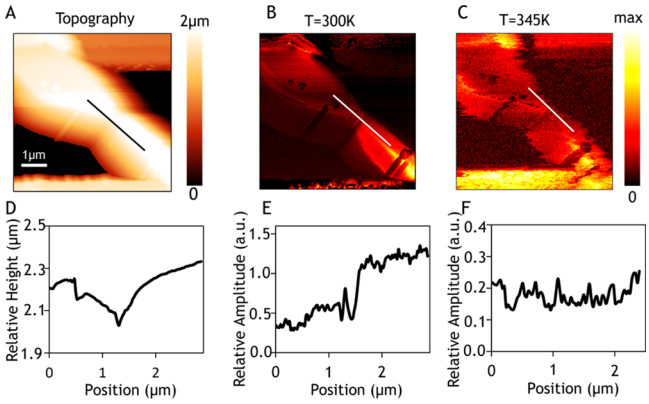

Figure 4. (A,D) AFM topography obtained via tapping mode on a suspended tapered VO_2 beam exhibiting 15% rectification at 300 K. The edges of the suspended membranes holding the beam are visible on the top and bottom of the image. A line profile is drawn across the tapered region on the beam with the relative height in μm illustrated in (D) as a function of beam length. (B) Near-field amplitude signal obtained at second harmonic demodulation at 300 K on the same tapered VO_2 beam. The black spots on the beam are dirt particles, possibly carbon, with a negligible dielectric value at the excitation frequency corresponding to a CO_2 laser wavelength of 10.7 μm. A white line profile is drawn across the taper with the corresponding line profile of the near field signal amplitude in (E). The near-field amplitude contrast changes significantly across the taper with the narrow region of the beam being more metallic and the broad section insulating. (C) The near field amplitude signal obtained on the same tapered VO_2 beam at 345 K, higher than the insulator–metal phase transition temperature of VO_2. The black spots, which are impurities on the surface, remain dark in contrast indicating temperature-independent contrast. A white line is drawn at the same location as that in (B) across the taper with its corresponding near field amplitude line profile illustrated in (F). The metal–insulator contrast difference seen in (E) at 300 K across the taper disappears at this higher temperature of 345 K, illustrating that the phase transition has occurred and that the phase is homogeneously metallic.

rectification at 300 K (data not shown in Table 1 as device broke before reaching 340 K during measurement), there exists s-SNOM amplitude contrast across the taper confirming phase coexistence at the same temperature (Figure 4B,E), which disappears when the sample is heated up to 345 K (Figure 4C,F). Note that the s-SNOM images show on average that the narrow side of the tapered VO_2 beam is metallic, while the broader side is insulating. Because the resolution is limited to ~30 nm, we did not observe any crystallographic shear planes with this technique. A similar experiment on a uniform cross-section beam shows no amplitude contrast evolution (Supporting Information 6).

While the s-SNOM figure (Figure 4B,C) shows unequivocally the presence of asymmetric mixed phases, the origin of these remains to be ascertained. As explained above, these could be due to a variation of stoichiometry along the beam length. We also found a signature of mixed vanadium oxide phases in tapered beams using auger electron spectroscopy (AES) (Supporting Information 7). In addition to stoichiometry, recent work shows that the phase transition also depends on stress fields within single VO_2 beams.[22] It is possible that the taper created during the beam growth may lead to stress gradients that could produce geometrical and size distributions of metallic and insulating domains and interfaces near the taper. These can amplify the rectification achieved by single interfaces. Similar distributions were previous reported by bending the beam.[19] Hence, while the insulator-to-metal phase transition is critical to thermal rectification, the taper and composition variation may also contribute to the effect by unique distributions of metal–insulator domains. On the basis of the interfacial thermal conductance from the two-temperature model described earlier,[30] we have estimated the approximate effective metal–insulator interface area required to observe the thermal rectification (details in Supporting Information 9).

The metal–insulator domains and interfaces can be rationally engineered to control the thermal transport. In stoichiometric VO_2 beams, an array of metal domains can be created below 340 K by either substitutional doping[35,36] or local stressing.[19,22] In addition, metal domains can be stabilized along these VO_2 beams at sub-340 K temperatures by encoding stoichiometry variation during the growth[21] or postgrowth hydrogenation.[37] Over the last several decades, while tremendous progress has been made in understanding the complexity of the phase transition in the family of vanadium oxides, the underlying physics still remains largely elusive.[38] Its impact on thermal transport is much less explored and has yet to be fully understood. Rational synthesis of vanadium oxide based beams with controlled local stresses and/or stoichiometry with a lack or excess of oxygen can open up pathways to further manipulate heat transfer in these systems.

In summary, we report a large thermal rectification up to 28% in VO_2 beams that is gated by the environmental temperature. It is the first demonstration of an active three-terminal thermal device exhibiting an "on" rectifying state over a large range of temperature (T_G = 250–340 K) and "off" resistor state (T_G < 250 K or T_G > 340 K). By changing temperature, one can switch the rectification, much like a gate voltage switches a thyristor between two states of electrical conductance. The realization of such unique thermal control is a consequence of the interplay between metallic and insulating phases due to the rich parameter space provided by the vanadium–oxygen material family. Such novel all-thermal devices may spurn interesting applications in autonomous thermal flow control and efficient energy harvesting.

■ ASSOCIATED CONTENT

Supporting Information

Details about synthesis of VO_2 nanowires, measurement, Auger Spectroscopy, additional data, and discussion and error analysis. This material is available free of charge via the Internet at http://pubs.acs.org.

■ AUTHOR INFORMATION

Corresponding Authors

*E-mail: (X.Z.) xiang@berkeley.edu.
*E-mail: (A.M.) 4majumdar@gmail.com.

Author Contributions

‖J.Z. and K.H. contributed equally.

Notes

The authors declare no competing financial interest.

■ ACKNOWLEDGMENTS

This work was supported by the U.S. Department of Energy, Basic Energy Sciences Energy Frontier Research Center (DoE-LMI-EFRC) under award DOE DE-AC02-05CH11231. This

materials synthesis part was supported by the U.S. Department of Energy Early Career Award DE-FG02-11ER46796. Y.A. acknowledges support from the U.S. Army Research Office, Agreement Number: W911NF-12-1-0076.

REFERENCES

(1) Fourier, J. B. J. *Théorie analytique de la chaleur*; Chez Firmin Didot Père et Fils: Paris, 1822.
(2) Ohm, G. S. *Die galvanische kette: mathematisch*; T. H. Riemann: Berlin, 1827.
(3) Chu, S.; Majumdar, A. *Nature* **2012**, *488*, 294−303.
(4) Li, B.; Wang, L.; Casati, G. *Phys. Rev. Lett.* **2004**, *93*, 1−4.
(5) Li, N.; Ren, J.; Wang, L.; Zhang, G.; Hänggi, P.; Li, B. *Rev. Mod. Phys.* **2012**, *84*, 1045−1066.
(6) Xie, R.; Bui, C. T.; Varghese, B.; Zhang, Q.; Sow, C. H.; Li, B.; Thong, J. T. L. *Adv. Funct. Mater.* **2011**, *21*, 1602−1607.
(7) Chang, C. W.; Okawa, D.; Majumdar, A.; Zettl, A. *Science* **2006**, *314*, 1121−1124.
(8) Roberts, N. A.; Walker, D. G. *Int. J. Therm. Sci.* **2011**, *50*, 648−662.
(9) Dames, C. *J. Heat Transfer* **2009**, *131*, 061301.
(10) Jezowski, A.; Rafalowicz, J. *Phys. Status Solidi* **1978**, *47*, 229−232.
(11) Yang, N.; Zhang, G.; Li, B. *Appl. Phys. Lett.* **2009**, *95*, 033107.
(12) Xia, Y.; Yang, P.; Sun, Y.; Wu, Y.; Mayers, B.; Gates, B.; Yin, Y.; Kim, F.; Yan, H. *Adv. Mater.* **2003**, *15*, 353−389.
(13) Cui, Y.; Wei, Q.; Park, H.; Lieber, C. M. *Science* **2001**, *293*, 1289−1292.
(14) Wang, Z. L.; Song, J. *Science* **2006**, *312*, 242−246.
(15) Hochbaum, A. I.; Chen, R.; Delgado, R. D.; Liang, W.; Garnett, E. C.; Najarian, M.; Majumdar, A.; Yang, P. *Nature* **2008**, *451*, 163−167.
(16) Boukai, A. I.; Bunimovich, Y.; Tahir-Kheli, J.; Yu, J.-K.; Goddard, W. a; Heath, J. R. *Nature* **2008**, *451*, 168−171.
(17) Xiang, J.; Vidan, A.; Tinkham, M.; Westervelt, R. M.; Lieber, C. M. *Nat. Nanotechnol.* **2006**, *1*, 208−213.
(18) Starr, C. *Physics (College. Park, MD)* **1936**, *7*, 15−19.
(19) Cao, J.; Ertekin, E.; Srinivasan, V.; Fan, W.; Huang, S.; Zheng, H.; Yim, J. W. L.; Khanal, D. R.; Ogletree, D. F.; Grossman, J. C.; Wu, J. *Nat. Nanotechnol.* **2009**, *4*, 732−737.
(20) Wei, J.; Wang, Z.; Chen, W.; Cobden, D. H. *Nat. Nanotechnol.* **2009**, *4*, 420−424.
(21) Zhang, S.; Chou, J. Y.; Lauhon, L. J. *Nano Lett.* **2009**, *9*, 4527−4532.
(22) Wu, J.; Gu, Q.; Guiton, B. S.; Leon, N. P.; De Ouyang, L.; Park, H. *Nano Lett.* **2006**, *6*, 2313−2317.
(23) Cavalleri, A.; Tóth, C.; Siders, C.; Squier, J.; Ráksi, F.; Forget, P.; Kieffer, J. *Phys. Rev. Lett.* **2001**, *87*, 1−4.
(24) Qazilbash, M. M.; Brehm, M.; Chae, B.-G.; Ho, P.-C.; Andreev, G. O.; Kim, B.-J.; Yun, S. J.; Balatsky, a V; Maple, M. B.; Keilmann, F.; Kim, H.-T.; Basov, D. N. *Science* **2007**, *318*, 1750−1753.
(25) Oh, D.-W.; Ko, C.; Ramanathan, S.; Cahill, D. G. *Appl. Phys. Lett.* **2010**, *96*, 151906.
(26) Kodambaka, S.; Tersoff, J.; Reuter, M. C.; Ross, F. M. *Science* **2007**, *316*, 729−732.
(27) Shi, L.; Li, D.; Yu, C.; Jang, W.; Kim, D.; Yao, Z.; Kim, P.; Majumdar, A. *J. Heat Transfer* **2003**, *125*, 881−888.
(28) Berglund, C.; Guggenheim, H. *Phys. Rev.* **1969**, *185*, 1022−1033.
(29) Maurer, D.; Leue, A.; Heichele, R.; Mu, V. *Phys. Rev. B* **1999**, *60*, 249−252.
(30) Majumdar, A.; Reddy, P. *Appl. Phys. Lett.* **2004**, *84* (23), 4768−4770.
(31) Zhang, L.; Lü, J.-T.; Wang, J.-S.; Li, B. *J. Phys.: Condens. Matter* **2013**, *25*, 445801.
(32) Wells, A. F. *Structural Inorganic Chemistry*; Oxford Classic Texts in the Physical Sciences; OUP: Oxford, 2012.
(33) Kachi, S.; Kosuge, K.; Okinaka, H. *J. Solid State Chem.* **1973**, *6*, 258−270.
(34) Jones, A. C.; Berweger, S.; Wei, J.; Cobden, D.; Raschke, M. B. *Nano Lett.* **2010**, *10*, 1574−1581.
(35) Lee, S.; Cheng, C.; Guo, H.; Hippalgaonkar, K.; Wang, K.; Suh, J.; Liu, K.; Wu, J. *J. Am. Chem. Soc.* **2013**, *135*, 4850−4855.
(36) Gu, Q.; Falk, A.; Wu, J.; Ouyang, L.; Park, H. *Nano Lett.* **2007**, *7*, 363−366.
(37) Wei, J.; Ji, H.; Guo, W.; Nevidomskyy, A. H.; Natelson, D. *Nat. Nanotechnol.* **2012**, *7*, 357−362.
(38) Tao, Z.; Han, T.-R.; Mahanti, S.; Duxbury, P.; Yuan, F.; Ruan, C.-Y.; Wang, K.; Wu, J. *Phys. Rev. Lett.* **2012**, *109*, 1−5.

Supporting Information for Temperature Gated Thermal Rectifier for Active Heat Flow Control

Jia Zhu[1Θ], Kedar Hippalgaonkar[1Θ], Sheng Shen[1], Kevin Wang[2], Yohannes Abate[3], Sangwook Lee[2], Junqiao Wu[2], Xiaobo Yin[1], Arun Majumdar[1#], Xiang Zhang[1#]

[1]Department of Mechanical Engineering, University of California at Berkeley, Berkeley, CA 94720, USA.
[2]Department of Materials Science and Engineering, University of California at Berkeley, Berkeley, CA 94720, USA.
[3]Department of Physics and Astronomy, Georgia State University, Atlanta, GA 30303 USA

Corresponding Authors: E-mail: xiang@berkeley.edu and 4majumdar@gmail.com

Author Contributions: [Θ] These authors contributed equally

1. Methods

Synthesis of VO_2 beams

Bulk VO_2 powder was placed in a quartz boat in the center of a horizontal tube furnace. The typical growth temperature was 1000 ºC with Ar used as the carrier gas. The VO_2 beams were collected on a Si substrate with a 500nm thick thermally grown surface oxide downstream from the source boat. The catalyst, which determines the size of the beam, can be partially diffused away by tuning the pressure and temperature to induce tapered or asymmetrical beam growth.

2. Thermal Conductance Measurement of Single VO_2 Beam

A resistive heater is used to heat the whole Si chip uniformly inside a cryostat to control the global device temperature, T_G. For thermal conductance measurements, a small DC

current (~6 μA) is passed through the platinum (Pt) coil on one of the membranes to heat it to a temperature, T_h, above T_G, thus inducing a heat flow Q through the VO_2 beam to heat up the other membrane to T_s. An AC current of 500 *nA* is passed through the Pt coils on both membranes to determine its electrical resistance through a 4-point technique, which is then used to estimate the temperatures T_h and T_s. Using two SRS 850 lock-in amplifiers for the AC signals, signals from the sensing side were measured using a frequency of 199 Hz whereas that for the heating side utilized 1.11 kHz. Details of the experimental procedure can be found elsewhere [1,2], while the error analysis from this experimental procedure is discussed later in the Supplementary Information. The resistance of the patterned coils, R_h and R_s varies between 3 and 5 kΩ at room temperature for different devices and is proportional to the temperature of the pads. Following the analysis of Shi et. al. [1], the thermal conductance of the Platinum beams that suspended each platform can be described as follows:

$$G_l = P \Big/ \left(\Delta T_h + \Delta T_s\right) \qquad \text{(SI 1)}$$

Here, a known power P was supplied to the Pt coil heater on one SiN_x membrane which also takes into account heat losses through the supporting legs, while resistance changes of the heater and sensor were used to determine the resulting temperature changes of the heater ($\Delta T_h = T_h - T_G$) and sensor ($\Delta T_s = T_s - T_G$) pads. Again following careful heat transfer analysis accounting for uniform joule heating in the Silicon Nitride (SiN_x) legs that suspended the platforms [1,2], it can be shown that $P = I_h^2\left(R_h + R_{leg}\right)$. Here I_h is the DC current supplied, $R_h \sim 3k\Omega$ is the resistance of the Platinum coil on the heating side and $R_{leg} \sim 3k\Omega$ is the electrical resistance of one out of six SiN_x legs that help suspend each

platform. At 300K, we can estimate that the heat loss through the SiN_x legs using the equation (SI 1) is $G_l \sim 100 nW/K$.

For an actual thermal device where the heating current is 6 μA, $R_h = 3.336 k\Omega$, $R_l = 3.340 k\Omega$, with a VO_2 beam placed across the heating and sensing pads, we obtain $\Delta T_h = 2.49K$ and $\Delta T_s = 0.96K$, which results in a leg conductance of $G_l = 69.5 nW/K$. Note here that using a 500 nA rms AC current on the heating and sensing pads to measure the resistances thus only gives a temperature rise on either membrane of $\Delta T_{h,AC} = \Delta T_{s,AC} \sim 10mK$, which is below the temperature fluctuations in the cryostat and only causes an additional increase in temperature excursion of $\Delta T_{AC}/\Delta T_s \sim 10mK/1K \sim 1\%$. Further, the heat flow through the VO_2 beam, Q can be determined as a function of $\Delta T = T_h - T_s$, which is typically maintained close to $1K$. The thermal conductance G of the VO_2 beams can hence be determined from ΔT_h and ΔT_s with the use of the relation

$$G = \frac{P}{\Delta T_h - \Delta T_s}\left(\frac{\Delta T_s}{\Delta T_h + \Delta T_s}\right) \qquad \text{(SI 2)}$$

The DC power input, P is known to a very high accuracy (<0.5%), while the temperature measurement uses the temperature coefficient of resistivity (TCR) of the Platinum thin film on either membrane(<2%) (see below for error analysis). The thermal measurement technique only measures a two-probe conductance, which includes the thermal contact resistance between the beams and the membrane. The contact resistance is shown to be negligible and in the limiting case, contributing insignificantly to the rectification behaviour (see below for details).

3(a). Heat flow and heat flow deviation as a function of temperature difference across a uniform VO2 beam at 300K and 360K

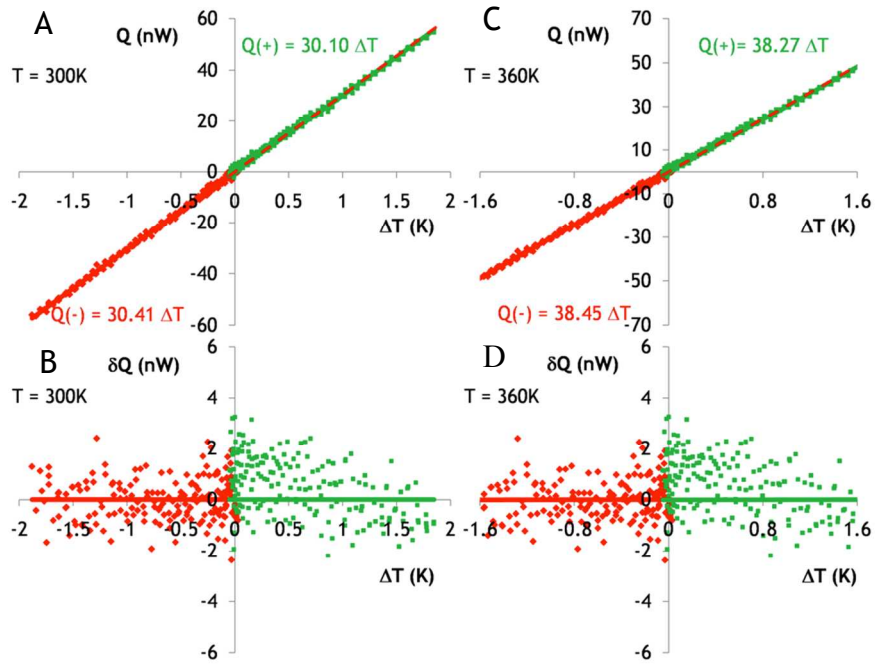

Fig. S1 A) and C) Heat flow (Q) as a function of temperature difference (ΔT) across the uniform VO_2 beams at 300K and 360K respectively. Different signs (+) and (-) of thermal power (Q) represent different directions of heat transfer. B) and D) Heat flow deviation (δQ) from linear fit as a function of temperature difference (ΔT) across the VO_2 beams at 300K and 360K correspondingly.

3(b). Temperature dependent conductance for a uniform VO_2 beam without rectification

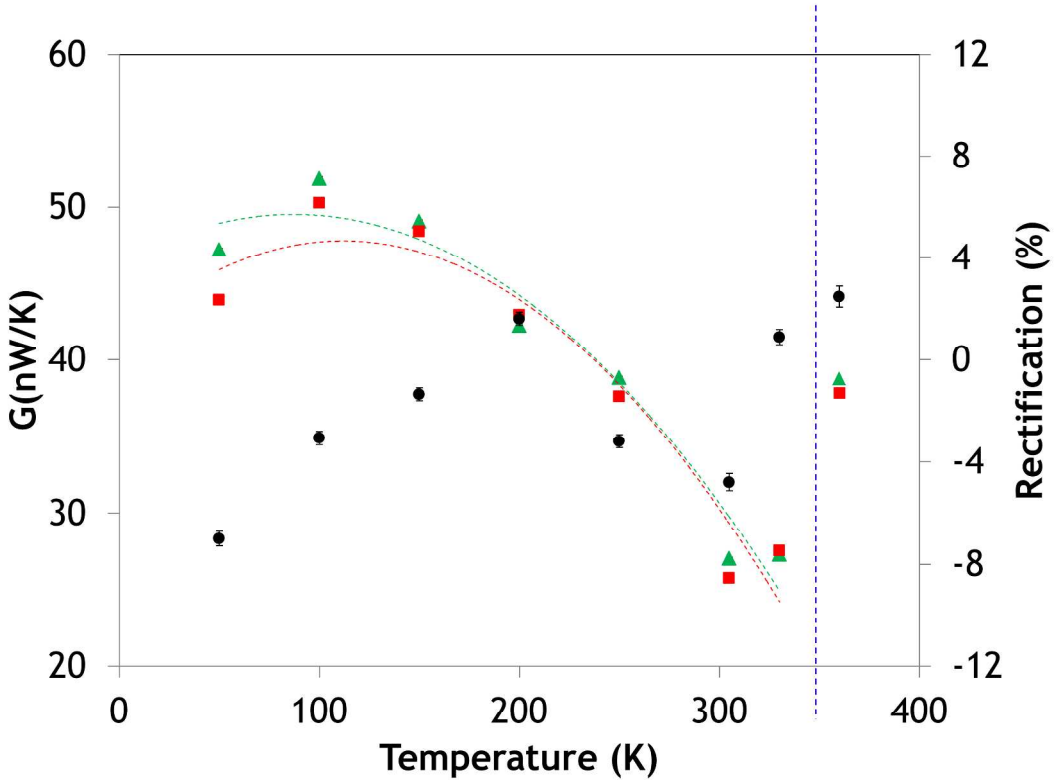

Fig. S2 Thermal conductance of a uniform VO_2 beam (the same as SI section 2(a)) along two opposite directions (green and red filled squares) as a function of global temperature. Also shown is the corresponding thermal rectification (black closed circles) that suggests no appreciable rectification. Note the phase transition temperature of 340K shown by a vertical blue dashed line.

4(a). Temperature dependent conductance for an asymmetrical VO_2 beam showing rectification – Beam II in main manuscript (Table I)

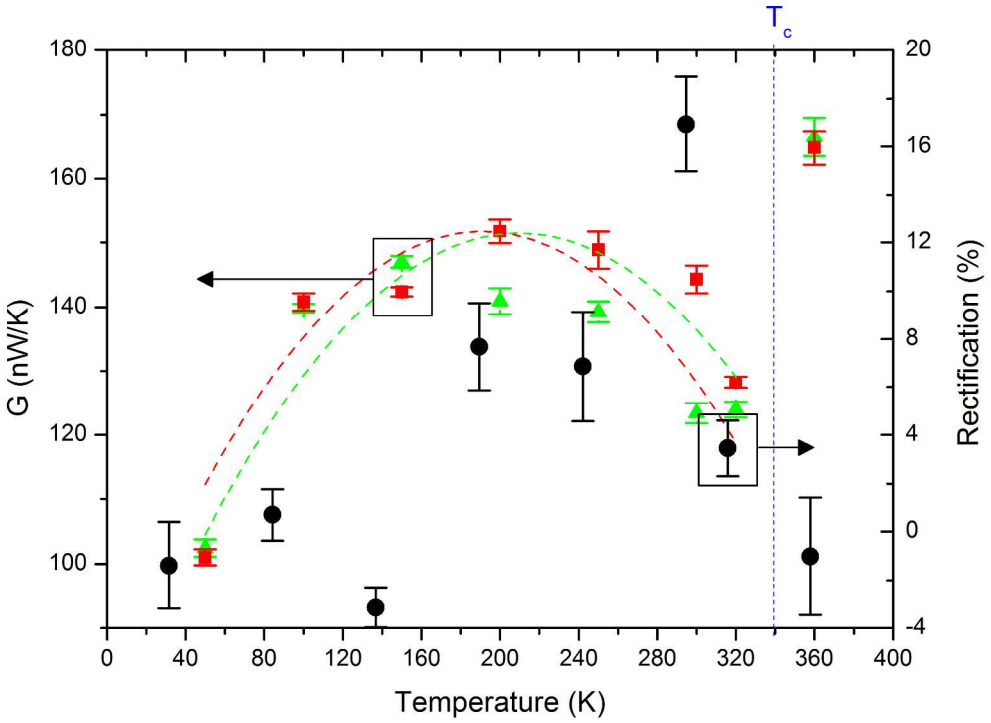

Fig. S3 Thermal conductance of the VO_2 beam II (see Table 1 in main manuscript) as a function of global heating temperature along two opposite directions, represented by two different symbols (green triangular and red squares). Also shown is the rectification (closed black circles) and its corresponding error bar. Thermal rectification ranges from 8 $\pm$1 % up to 16$\pm$1.2% in the temperature range from 200 to 340K.

4(b). Temperature dependent conductance for Beams III-VI in the main manuscript (Table I)

Beam III and IV:

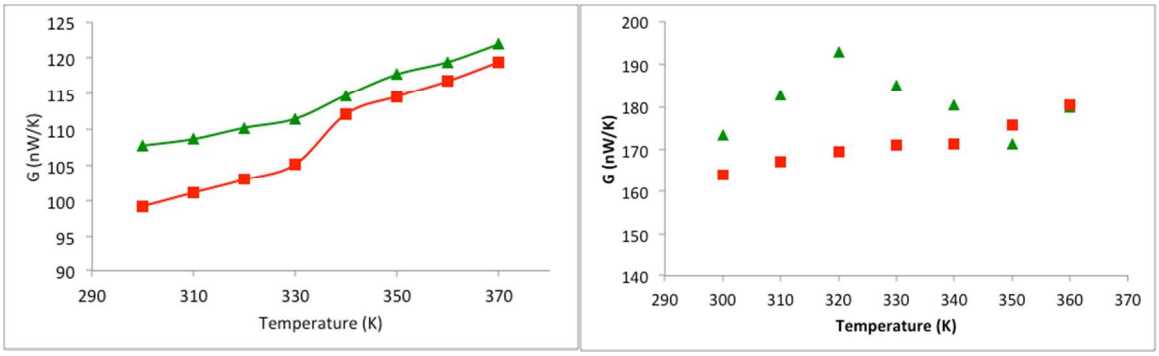

Beam V and VI:

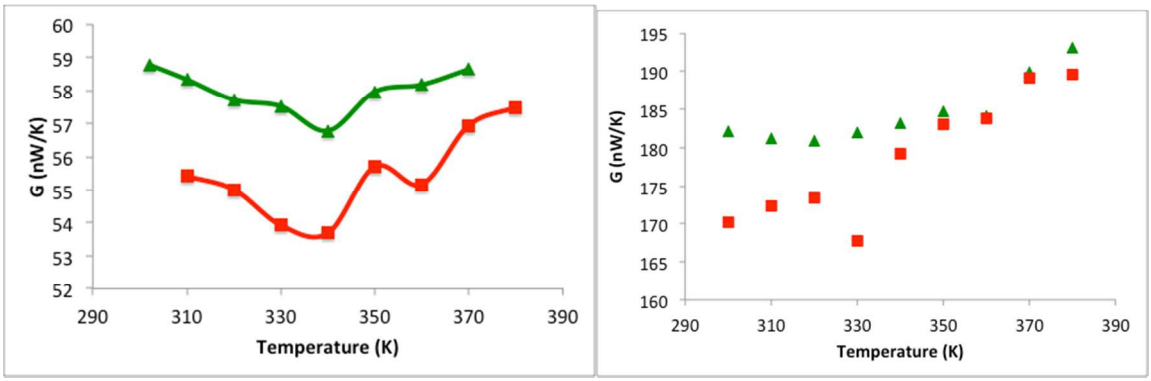

Fig. S4 Temperature Dependent Conductance of Beams III-VI in the main manuscript (Table I). Rectification in Beam V does not switch off in the purported fully-metallic phase. The temperature dependence of conductance is different for different beams and we hypothesize that this is due to the conflicting effect of phonon scattering and interfaces.

5. Electrical Measurement on VO_2 beams

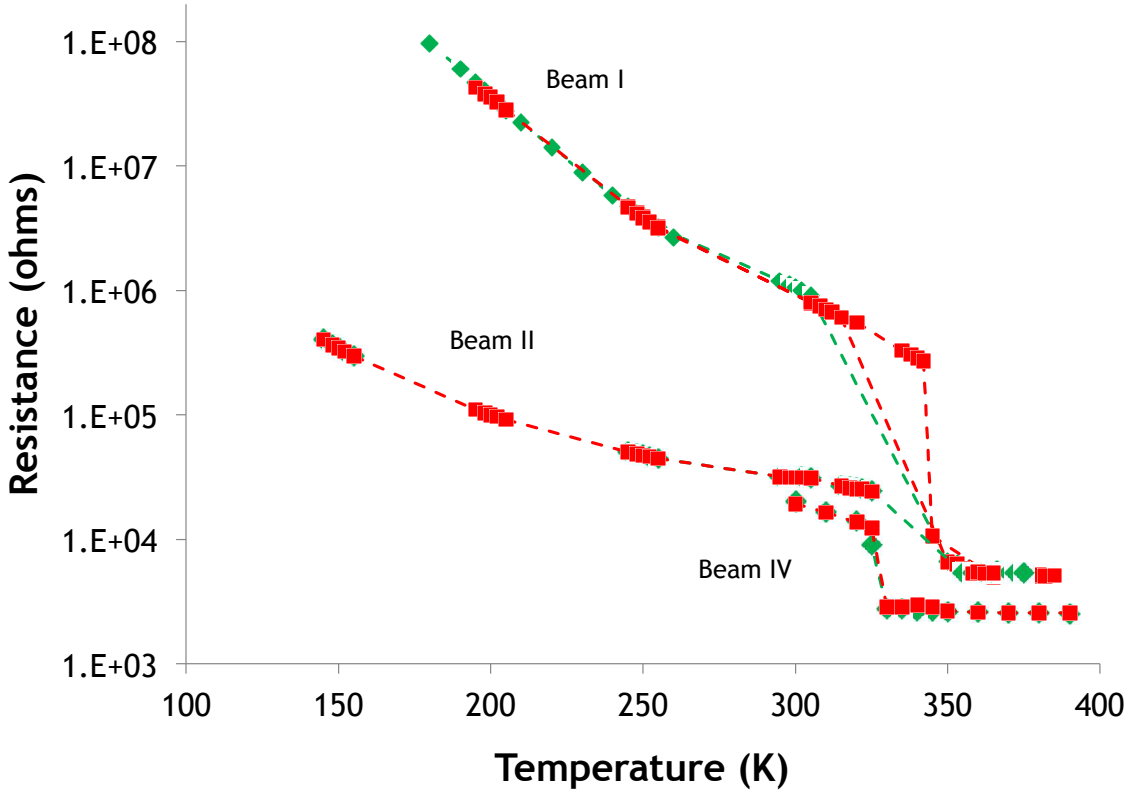

Fig. S5 Electrical resistance of three asymmetrical VO_2 beams as a function of global heating temperature, showing the electrical phase transition at 340K. It is a two probe measurement performed at the same temperature as the thermal conductance measurement. Except for the temperatures close to phase transition, the electrical rectification is below 1%.

6. Near-field Infrared Spectroscopic Study on VO_2 Beams

Near-field infrared spectroscopic imaging was performed with a (scattering type scanning near-field microscope (s-SNOM) which is based on a tapping mode AFM. Vertically vibrating PtIr-coated Si-tip (apex radius $R \approx 20$ nm) with an amplitude of about 25-30 nm at a frequency of $\Omega \approx 280$ kHz is illuminated by a focused CO_2 laser beam at wavelength, λ=10.7 μm. The tip converts the illuminating radiation diffraction limited spot into a highly localized and enhanced near field at the tip apex. Due to the near-field interaction between tip and sample, the back-scattered radiation from the probe tip is modified in both amplitude and phase, commensurate to the local dielectric response of the sample. [3,4] The tip-scattered light is detected using a pseudo-heterodyne interferometric detection scheme, which enables simultaneous recording of amplitude and phase of the scattered field [3–5]. Background signals are efficiently suppressed by demodulating the detector signal at the second harmonic of the tip oscillating frequency.

The contrast formation in s-SNOM near-field imaging of metal-insulator transition (MIT) in VO_2 is understood by considering the scattered signal at the second harmonic of the tip frequency as a function of the optical constants of the tip and the sample. Metallic regions show higher scattering amplitude owing to large negative real part and large positive imaginary part of the optical constants at λ=10.7 μm. Insulating regions have lower scattering amplitudes because of the small imaginary and real part of the optical constants. This difference in locally varying optical constants, and thus s-SNOM scattering amplitude signal, provides the basis for image contrast formation of the metal and insulating phases in VO_2.

We directly observe the nanoscale spatial evolution of one phase to another of a tapered crystal VO_2 beam grown on SiO_2 as shown in figure S6. Fig. S6a shows the topography of the taper, s-SNOM second harmonic optical amplitude images recorded at several temperatures are shown in figure S6b-d.

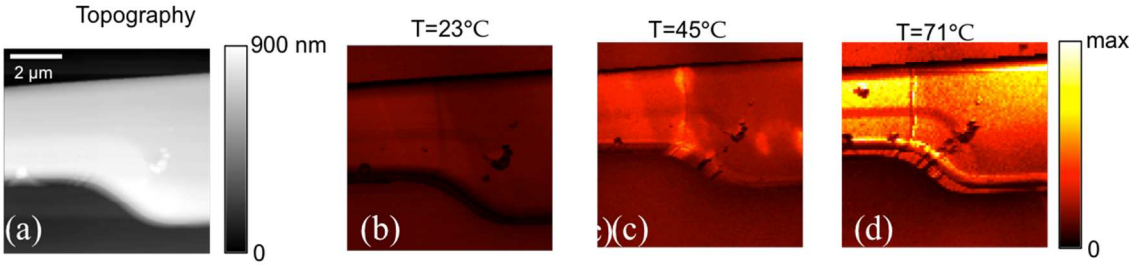

Fig. S6 Topography (a), s-SNOM second harmonic optical amplitude images (b-d) recorded at several temperatures at selected laser wavelength, λ=10.7 μm.

We selected to perform s-SNOM direct imaging of VO_2 beam at laser wavelength, λ=10.7 μm because the dielectric constant of the insulating and metallic phases of VO_2 display significant differences at this wavelength that allow strong s-SNOM optical contrast. As discussed in the main text the thinner part of the taper generates brighter contrast than the wider side suggesting phase coexistence even at room temperature. As temperature is increased, inhomogeneous mixed phase dynamics across the taper is observed until the phase transition is more complete at higher T leading to a more uniformly bright near-field contrast. As described in literature, the stress due to the underlying substrate can affect phase nucleation in VO2. Hence, we use a freestanding suspended beam in Figure 4 in the main manuscript to illustrate a similar qualitative effect to demonstrate co-existence of the metallic and insulating phases at room temperature.

We have also performed s-SNOM on straight suspended VO_2 beams. Figure S7 shows the topography and near-field amplitude images of a straight suspended VO_2 beam. Unlike a tapered beam, which displays s-SNOM amplitude contrast at room temperature, the contrast in Fig. S7 evolves uniformly across the rod displaying an overall stronger signal, but no variation in contrast along the line profile in the metallic phase (71 C, Fig. S7c) compared to the insulating phase (26 C, Fig. S7b).

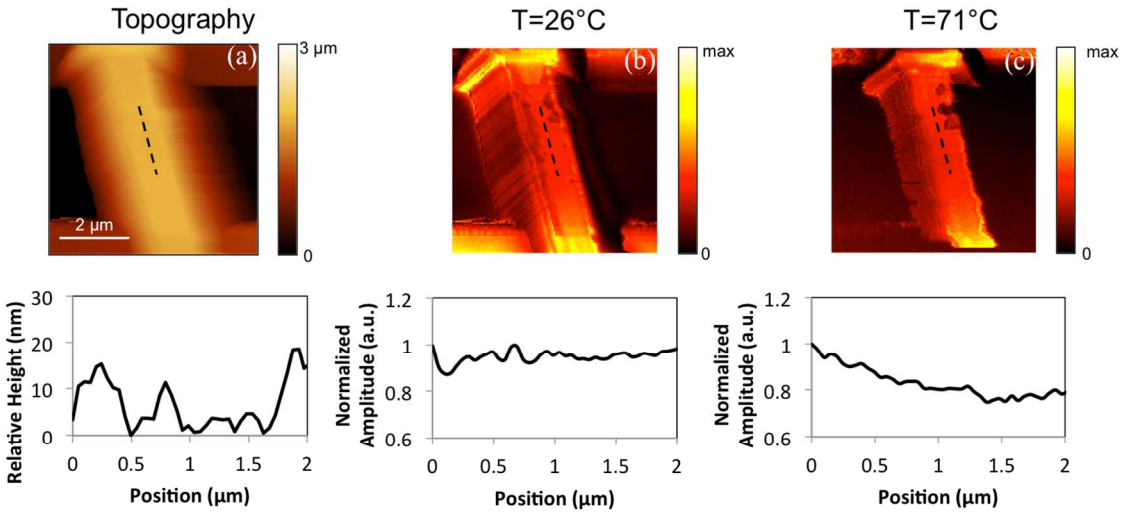

Fig. S7. Topography (a) and near-field amplitude images (b-c) of a straight suspended VO_2 beam. Unlike a tapered beam, which displays s-SNOM amplitude contrast at room temperature, the contrast in Fig S8 evolves uniformly across the rod displaying strong contrast in the metallic phase (71 C, Fig. S7c) compared to the insulating phase (26 C, Fig. S7b).

7. Auger Electron Spectra for Composition Analysis

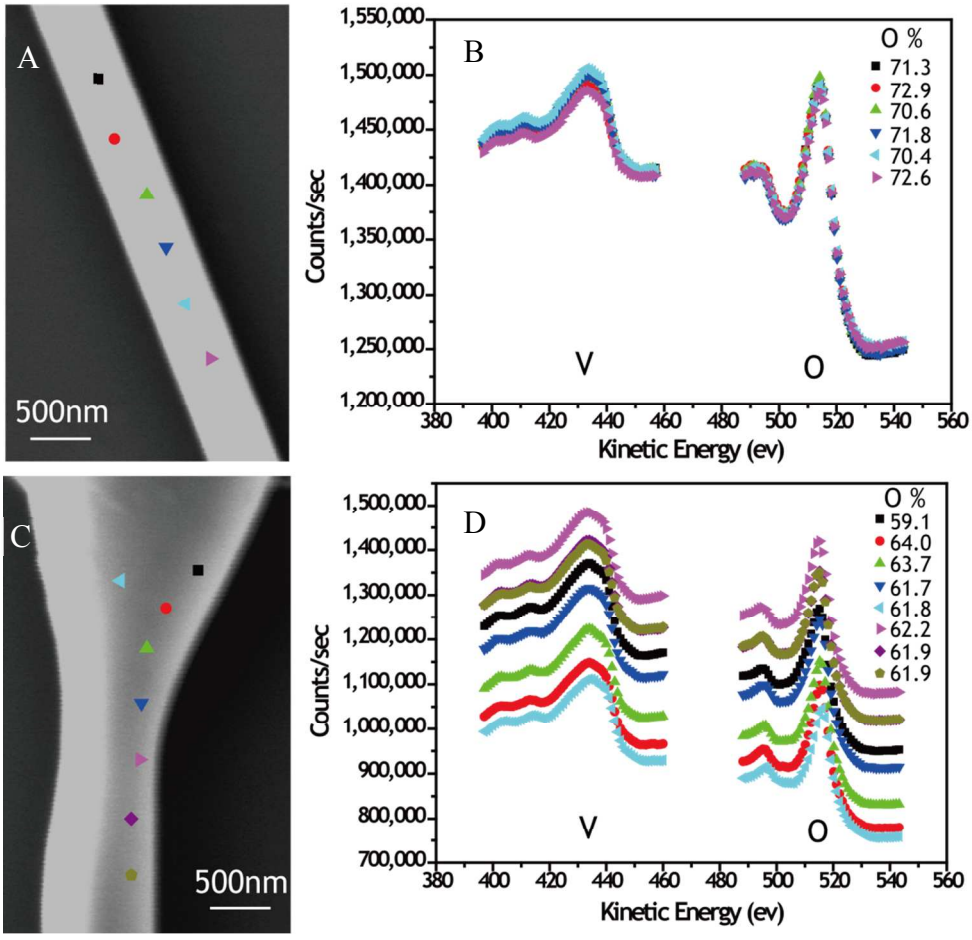

Fig. S8 A) Scanning Electron Microscopy (SEM) image of a uniform VO_2 beam, where the colored symbols represent locations used (~10nm resolution) for stoichiometric analysis. B) Auger Electron Spectra for the uniform VO_2 beam, with different colors representing the places labeled in A). C) Scanning Electron Microscopy (SEM) image of an asymmetric VO_2 beam, where the colored symbols represent places for stoichiometric analysis. D) Auger Electron Spectra for the asymmetric VO_2 be=am, where the different colors represent the places labeled in C).

It is observed that the oxygen composition on the surface of the uniform beam is higher than 66.7% (as in VO_2). This oxygen-rich surface can be attributed to the general oxygen rich environment, as the beams are exposed to air during storage. It has been demonstrated in literature that exposing bulk VO_2 single crystals to an oxygen environment can produce surface oxidation tending towards V_2O_5 (71.4% oxygen) [6]. Such a study has not been performed on VO_2 beams grown using our techniques, but given the larger surface-to-volume ratio of such nano/micro scale beams, it is highly likely that the surface of the VO_2 beams in our study is oxygen-rich. Interestingly, it is observed that the oxygen composition on the surface of an asymmetric beam is lower than 66.7% (Fig. S8 (D)), despite the general oxygen rich environment. As discussed in

the main manuscript, the phase transition temperature is very sensitive to the stoichiometry of V_nO_{2n-1}. Hence, we expect these oxygen-deficient spots to remain in a metallic phase over a large range of temperatures (down to 135K for V_2O_3) [7,8].

8. The Impact of Thermal Contact Resistance

Since we measure the two-probe thermal conductance of the VO_2 beam, it is impossible to eliminate the effect of thermal contact resistance. The contribution of contact resistance between the nanobeam and the suspended membrane to the total measured thermal resistance can vary depending not only on the quality of the contact, but also the temperature drop across the nanobeam itself [1]. Let's consider that the thermal conductivity of bulk VO_2 is ~4-6 W/m-K in the insulating phase at 300K [9–11]. The typical cross-section of the beams is rectangular with the width, w and height, h around 500nm to 1.5μm. Consider for example beam IV (see Table 1) in the manuscript. The geometry of the beam is drawn below:

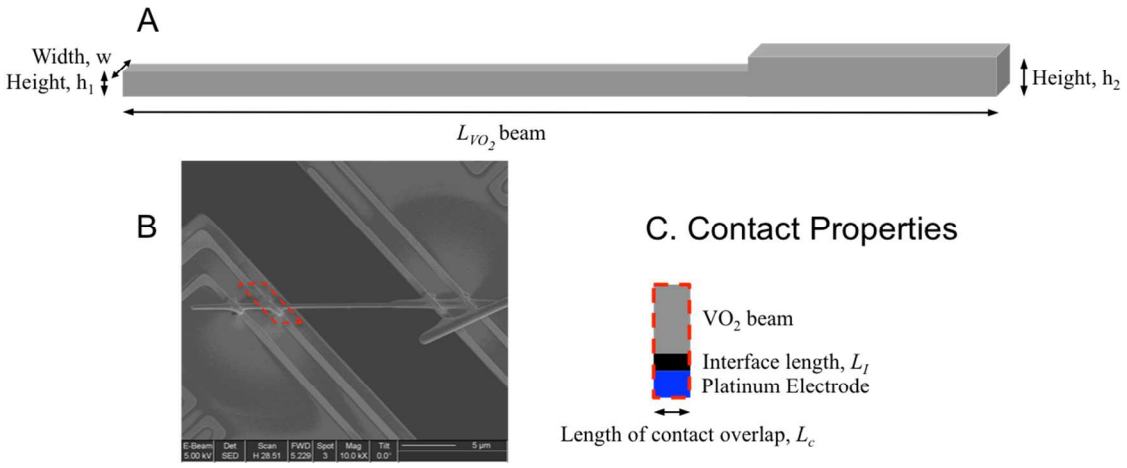

Fig. S9 A. A representation of the typical geometry of VO_2 beams used in this study. For beam IV (see Table 1 in main manuscript), w = 270 nm, h_1 = 510 nm, h_2 = 820 nm, L_{VO_2} = 13.7 μm B. Top view Scanning Electron Micrograph of beam IV showing the asymmetrical geometry and Pt/C Focused Ion Beam Induced Deposits (FIBID) to improve thermal contact resistance and also provide electrical contact to the Platinum electrodes on the suspended membranes C. Cross-section diagram of each of four contacts between the VO_2 beam (grey) and the Platinum Electrode (blue) on the suspended membrane, with the interface (black). The length of the interface is defined as L_I, and the overlap between the VO_2 beam and the Platinum Electrode is defined as L_c.

Using an average cross-sectional area based on the dimensions shown above in Fig S9A, and approximating k = 5 W/m-K for the VO_2 beam, we expect the beam conductance to be 58.6 nW/K. The actual measured conductances G+ and G- are 56 and 48 nW/K respectively, which are agreeably close to the expected value. For other geometries of nanowires measured in this study, the range of measured thermal conductances is between 50 to 200 nW/K. This translates to the measured thermal resistance, $R_{th} = 1/G$ between the two pads of between 5 and 20 K/μW.

In order to estimate the effect of contact resistance, we follow the analysis in Yu et al. [12] and approximate the contacts between the beam and the membrane as rectangular fins. The thermal contact resistance R_c can be approximated as [13]:

$$R_c = \frac{1}{4} \cdot \frac{1}{\sqrt{hPkA_c}\tanh\left(\sqrt{hP/kA_c}\,L_c\right)} \qquad \text{(SI 3)}$$

where h (W/m^{2}K) is the lateral heat transfer coefficient between the VO_2 beam and Platinum contact on the pads, P=*width* is the effective perimeter of contacts performing as fins (the beam touches the membranes at the Platinum electrodes, each L_c in width as shown in Fig.S9C), k is the thermal conductivity of the VO_2 beam and A_c = *width*height* is the cross-sectional area of the beam. Let's approximate $h \approx k_I / L_I$ [12], where k_I is the estimated thermal conductivity and L_I is the length of the ill-defined interface between the VO_2 beam and the Pt electrodes on the suspended membrane, as illustrated by Fig S9C in black. In order to determine the maximum possible thermal contact resistance, R_c, let us consider the scenario where the interface is sandwiched between the VO_2 beam and the Platinum electrode, as illustrated in Figure S9C.

The unknowns in Equation SI 3 are thus: k_I and L_I. Also, the area of contact changes for different widths of the beam, w.

a) Interface conductivity, k_I: The worst scenario is all air contact, which is avoided by doing a tilted SEM and ensuring that the contact between the beam and Pt electrode is good. Once the FIBID based Pt/C composite is placed on the electrode, the area is observed with tilted SEM to be filled. Hence, the realistic lower limit is Pt/C composite with 30% Pt. This is an organometallic, with Pt particles joined by an organic substance [14] and is known to resemble metal powders with 30% porosity (air gaps), who have a lower limit of thermal conductivity of k_I =1 W/m-K [15]. In the other extreme, the best-case scenario in the limit of perfect contact, is the Pt thermal conductivity itself, which is 20-30 W/m-K depending on the grain sizes for thin film Platinum.

b) Length of the interface, L_I: The length of the contact can be approximated to span values from 1 nm to 100 nm as an extreme case.

Taking these length scales into considerations, Fig S10 shows the values of the thermal contact resistance (R_c) for different values of the unknown parameters:

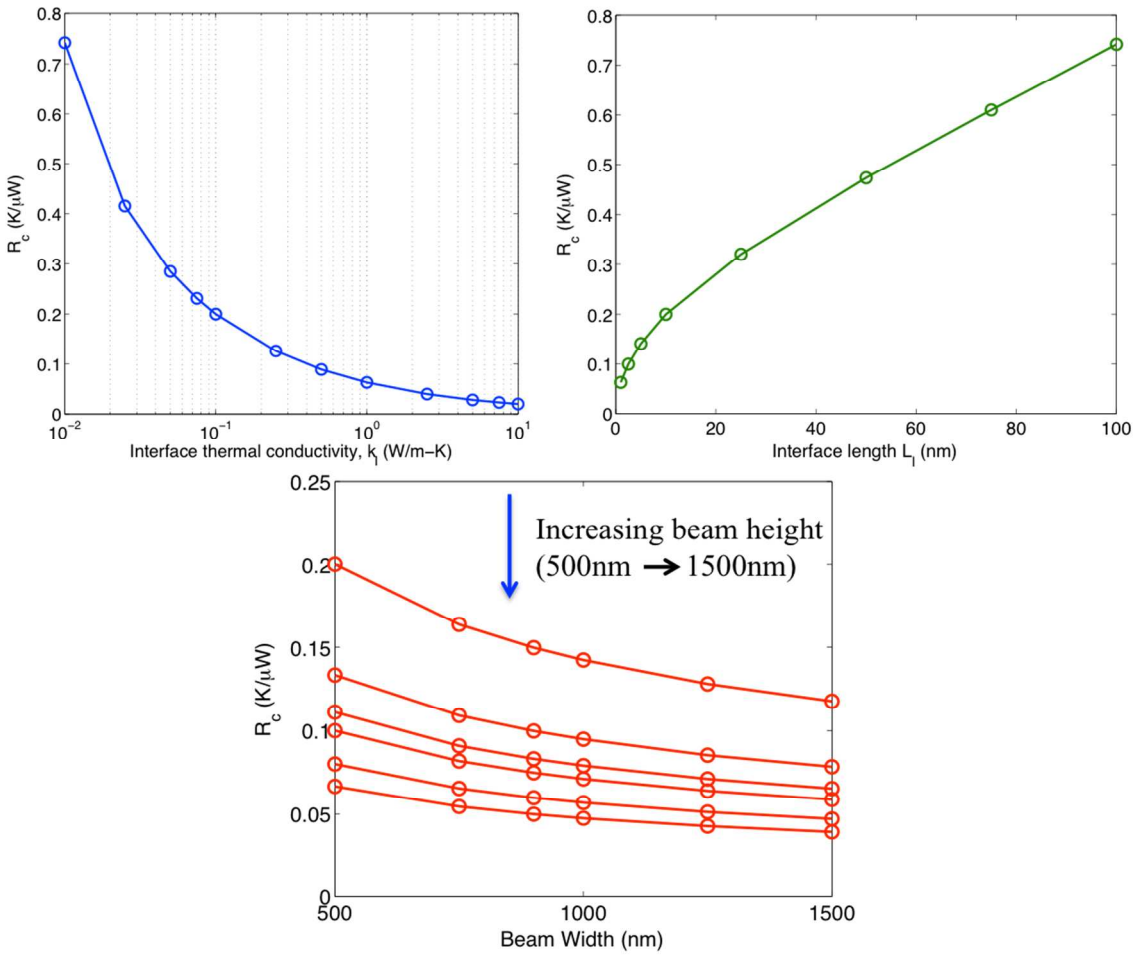

Fig. S10**A**. The thermal contact resistance, R_c as a function of the interface thermal conductivity, k_I approximating the contact area as a fin with adiabatic ends and a contact length of 1μm. The maximum R_c ~0.75 K/μW is when k_I = 0.01 W/m-K. For this graph, L_I = 10 nm, w = 500 nm and h = 500 nm. **B**. Predicted thermal contact resistance, R_c as a function of expected values of the interface length, L_I ranging from 1 to 100 nm where k_I = 0.1 W/m-K, w = 500 nm and h = 500nm. **C**. Predicted thermal contact resistance, R_c as a function of beam widths and heights ranging from 500 nm to 1.5 μm when k_I = 0.1 W/m-K and L_I = 10 nm.

In Fig. S10A, we have plotted R_c as a function of different k_I ranging from 0.01 W/m-K to 10 W/m-K. As can be seen from Fig. S10A, R_c is expected to be < 0.75 K/μW for a large area of contact, which is at most 15% of our measured resistance. Note that we have used a beam width and height of 500 nm and L_I = 10 nm. Fig. S10B shows the

effect that the interface length, L_I has on R_c. Even in the extreme case of L_I = 100 nm, assuming k_I = 0.1 W/m-K, we only get R_c ~ 0.75 K/μW. Finally, as expected, the contact resistance decreases as we increase the beam width upto 1.5 μm, as the area of contact increases as illustrated in Fig. S10C. Here, we assume k_I = 0.1 W/m-K and L_I = 10 nm.

Another way of estimating the contact resistance is by considering the thermal interface resistance reported in literature for highly dissimilar materials. Even in this limit, the smallest thermal interface conductance between two solids is given by G_c' ~ 10 MW/m^2-K [16]. Considering this value for the contact area in our system given by w = 500 nm, L_c = 1 μm, we obtain $R_c = 2 \cdot \frac{1}{G_c' A} < \frac{2}{\left(10 MW\, m^{-2}\ K^{-1} \cdot 500\, nm \cdot 1 \mu m\right)} = 0.4\, {}^{K}\!/_{\mu W}$, which is at most 8% of our measured thermal resistance.

Also note that this contact resistance only assumes direct contact between the VO_2 beam and the Platinum contacts via the Pt/C composite on the suspended pads. In practice, this is alleviated by the focused ion beam induced deposition (FIBID) of a Pt/C composite, which (1) increases the contact area between the VO_2 beam and the suspended membrane and (2) fills in any air gaps in the dry interface at the points of contact with the organometallic Pt/C substance. It has been shown previously that the total measured thermal resistance (including the contact) can be reduced by 10-15% by depositing this composite using the FIBID [12,17–19].

Further, we have used a non-tapered VO_2 beam whose geometry was carefully ascertained with cross-sectional SEM. The measured thermal conductance was 49.6 nW/K, R_{th} = 20.2 K/μW. The thermal conductivity matches that of bulk, k~5.5 W/m-K at room temperature, which indicates that when heat flows from the suspended membranes

into the nanowire, most of the temperature drop occurs across the beam and the discontinuity in temperature at the contact is small. Based on the analysis above and Fig. SI 10A, $R_c < 0.75$ K/μW, which is at most 2% of the measured resistance without considering the additional improvement in contact from the Focused Ion Beam Induced Deposition (FIBID) of Pt/C.

Next, we show below that the thermal contact resistance alone cannot explain the asymmetrical behavior of heat flow. Consider the case where the contact resistance has different temperature dependences at a particular gate temperature; this could result in rectification. Following the analysis of Dames, we can estimate an upper bound for thermal rectification due to contact resistance as shown in Figure 8(b) in the referenced manuscript, where the contacts are shown to dominate the thermal resistance across the two ends and the two contact 'segments' are labeled *1* and *2,* respectively. Specifically, using Equation *(24)* of the referenced manuscript, the rectification can be described as:

$$\gamma = \frac{n_1 - n_2}{\left(\rho^{1/2} + \rho^{-1/2}\right)^2}\Delta \qquad \text{(SI 4)}$$

where γ is the rectification, n_1 and n_2 are the temperature exponents that defines the temperature-dependence of thermal conductivity near gate temperature T_G for each contact segment, ρ is the ratio R_2/R_1 where R_i is the thermal resistance of each segment and $\Delta = \left(T_h - T_s\right)/T_G$ is a normalized temperature with respect to the gate temperature. If the contacts are treated as thin heat conductors, then $\left(n_1 - n_2\right) \le 6$. However, if the contacts are treated as a mismatch between the two materials at the contact, $\left(n_1 - n_2\right) \le 3$ (see Reference [20] for details). To maximize the rectification at a particular Δ, the

denominator needs to be minimized, which gives us $\rho = 1$. Then, for our experiments performed in the low-bias limit, where $\left(T_h - T_s\right) \leq 2K$ and $T_G \approx 300K$,

$$\gamma_{\max} \approx \frac{6}{4} \times \frac{2}{300} = 1\%.$$

In summary, first, the measured thermal conductances for all the VO_2 beams lie between 5 and 20 K/μW, with the maximum thermal contact resistance of 0.75 K/μW. This is expected to improve after Pt/C deposition using a FIB, which was also used to make electrical contact to the suspended VO_2 beam. The measured thermal conductivity (~5.5 W/m-K) of a uniform VO_2 beam indicates that the thermal contact resistance in our measurement is negligible since the measured value matches that of bulk. Secondly, even in the limiting case of thermal contact resistance dominating, for the low-bias experiment we have performed, maximum rectification in the system could atmost be 1%.

9. Estimation of Metal-Insulator Thermal Interface Resistance

If we consider electron-phonon inequilibrium at the Metal-Insulator interface, in the configuration illustrated below:

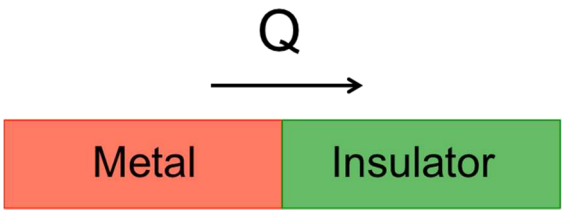

Here, the heat flows from the metal to the insulator. Using the two-temperature model as described in [21], the interface conductance, h_I can be defined as:

$$h_I = \frac{k_p \sqrt{\frac{G_{e-l}}{k_{hm}}}}{1 + \frac{k_p}{h_{pp}} \cdot \sqrt{\frac{G_{e-l}}{k_{hm}}} - \frac{k_{hm}}{k_e}} \qquad \text{(SI 5)}$$

where k_p and k_e are the phononic and electronic thermal conductivities on the metallic side and k_{hm} is the harmonic mean given by: $k_{hm} = \left(1/k_p + 1/k_e\right)^{-1}$, h_{pp} is the phonon-phonon interface conductance, and $G_{e\text{-}l}$ is the electron-phonon cooling rate. For a normal metal, $k_e >> k_p$. However, for VO2 we need three cases, when the total thermal conductivity is estimated as k_T= 10 $Wm^{-1}K^{-1}$.

(a) if Weidemann-Franz law is violated and k_e=0, then k_p = 10 $Wm^{-1}K^{-1}$and k_{hm} = 0 $Wm^{-1}K^{-1}$.

(b) If Weidemann-Franz law is valid, and $k_e = L\sigma T$=(2.44e-8).(1e6).(350) = 8.5 $Wm^{-1}K^{-1}$. Then, k_p = 1.5 $Wm^{-1}K^{-1}$ and k_{hm} = 1.275 $Wm^{-1}K^{-1}$.

(c) If there is equal contribution from the electrons and phonons to the total thermal conductivity, $k_e = k_p$ = 5 $Wm^{-1}K^{-1}$ and k_{hm} = 2.5 $Wm^{-1}K^{-1}$.

In the insulating state, $G_{e-l} \sim (0.1-3)e^{16}\ Wm^{-3}K^{-1}$ [22]. Also, since the lattice mismatch between the metallic and insulating state is very small, we can assume that the phonon-

phonon interface resistance is very high, $h_{pp} \sim 100\, MWm^{-2}K^{-1}$. Since $h_I \propto h_{pp}$, this assumption will give us a conservative over-estimate of the interface conductance. Then, using Equation (SI 5) and substituting values for all three cases, we find that h_I ranges from ~33 to 92 $MWm^{-2}K^{-1}$.

Now, consider our measured thermal conductance of the VO_2 beam to be $G_T = 100\, nWK^{-1}$, and hence total measured thermal resistance including the metal-insulator interface is given by $R_T = 1/G_T = 1e7\, KW^{-1}$. Since the total resistance is a series resistance of the metallic and insulating elements and the metal-insulator interface, if we assume that the observed thermal rectification comes purely from the metal-insulator interface, then for a rectification of 25%, the interface thermal resistance has to be given by: $R_I = 0.25 \cdot R_T = 2.5e6\, KW^{-1}$.

If we take this to be the measured interface resistance, then we can estimate how much area we need given the thermal interface conductance, h_I calculated above.
Then, $A_I = 1/h_I R_I$ gives an estimated effective-interface area $A_I \approx 4350 - 12120\, nm^2$. If we approximate this interface to be a square cross-section, then the lateral dimensions would be (~66x66) nm^2 up to (~110x110) nm^2. Of course, this estimate of the interface area depends upon the total measured thermal conductance and the rectification magnitude.

10. Error Analysis for Thermal Conductance Measurements

In the thermal measurement scheme, the conductance of the beam is determined by ramping up the temperature in a stepwise (50 steps) fashion by passing a DC current (0-8μA) through the PRT on the heating membrane. The rise in temperature on either side is monitored by measuring the resistances, R_s and R_h on both platforms, as seen in Fig S11 below. For a Platinum Resistance Thermometer (PRT) in the temperature range of our measurement (50K-300K), the resistance changes linearly with temperature:

$$\Delta R_s = \left(R_s - R_{s,G}\right) \propto \left(T_s - T_G\right) = \Delta T_s \text{ and } \Delta R_h = \left(R_h - R_{h,G}\right) \propto \left(T_h - T_G\right) = \Delta T_h$$

Since the rise in temperature is proportional to the supplied power through I_h,

$$\Delta T_h \propto I_h^2 R_{h,G} \; and \; \Delta T_s \propto I_h^2 R_{h,G}.$$

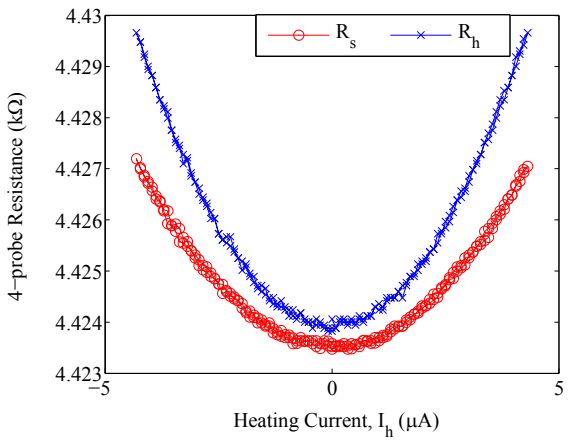

Fig. S11 R_s and R_h as a function of the heating current, I_h. Resistance is proportional to temperature, which in turn is proportional to the power supplied by joule heating. Thus, the resistance has a quadratic dependence on I_h

Following the analysis of Equation (SI 2), the heat flow in the VO_2 beam can be estimated as: $Q = \gamma \cdot \frac{I_h^2 R_h}{\left(\Delta T_h + \Delta T_s\right)} \cdot \Delta T_s$, where γ is a non-dimensional ratio of the resistance of the PRT and the resistance of the suspended legs. γ is a constant at all temperatures.

The beam conductance can then be determined using the relation $G = Q \big/ (\Delta T_h - \Delta T_s)$. Then, error propagation rules determine that:

$$\left(\frac{\delta Q}{Q}\right)^2 = 2 \cdot \left(\frac{\delta I_h}{I_h}\right)^2 + \left(\frac{\delta R_h}{R_h}\right)^2 + \left(\frac{\delta(\Delta T_s)}{\Delta T_s}\right)^2 + \left(\frac{\delta(\Delta T_h + \Delta T_s)}{\Delta T_h + \Delta T_s}\right)^2 \qquad \text{(SI 5)}$$

$$\text{and, } \left(\frac{\delta G}{G}\right)^2 = \left(\frac{\delta Q}{Q}\right)^2 + \left(\frac{\delta(\Delta T_h - \Delta T_s)}{\Delta T_h - \Delta T_s}\right)^2 \qquad \text{(SI 6)}$$

Hence, the following error terms need to be determined:

(1) $\frac{\delta R_h}{R_h}$, (2) $\frac{\delta(\Delta T_s)}{\Delta T_s}$, (3) $\frac{\delta(\Delta T_h + \Delta T_s)}{\Delta T_h + \Delta T_s}$ and (4) $\frac{\delta(\Delta T_h - \Delta T_s)}{\Delta T_h - \Delta T_s}$

The linear dependence of the PRT resistance with respect to temperature allows us to define ΔT_s and ΔT_h. One cycle of measurement constitutes gathering this raw data at 5 different local temperature points around T_G. Consider the partial derivative $\partial R_{h/s} \big/ \partial T_{h/s} \approx \Delta R_{h/s} \big/ \Delta T_{h/s}$ at T_G = 300K. Then, we measure the resistances $R_{s,G}$ and $R_{h,G}$ at 295K, 298K, 300K, 302K and 305K. The plot of resistance as a function of gate temperature is typically a line as below:

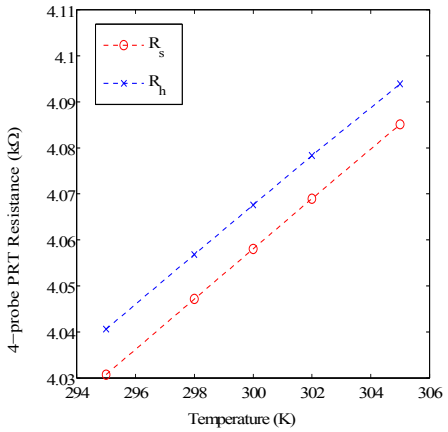

Fig. S12 Measured R_s and R_h around T_G=300K used for calibration of TCR.

If we define $\alpha_s \equiv dR_s/dT_G \sim \Delta R_s/\Delta T_G$ and $\alpha_h \equiv dR_h/dT_G \sim \Delta R_h/\Delta T_G$ then these slopes can be determined to very high accuracy. In general, $\delta\alpha_s/\alpha_s$ and $\delta\alpha_h/\alpha_h \leq 1.75\times10^{-2}$ when $R^2 >$ 0.9999 for the least squares fitting shown in Fig. S12 above. To understand where this error comes from, consider the following error propagation (where *i = h or s)*:

$$\left(\frac{\delta\alpha_i}{\alpha_i}\right)^2 = \left(\frac{\delta(\Delta R_i)}{\Delta R_i}\right)^2 + \left(\frac{\delta(\Delta T_i)}{\Delta T_i}\right)^2$$

Following the analysis of Shi [2], we have verified that $\frac{\delta R_i}{R_i} = \sqrt{\left(\frac{\delta v_{out}}{v_{out}}\right)^2 + \left(\frac{\delta i_{ac}}{i_{ac}}\right)^2} \approx 5\times10^{-5}$ from the AC measurements of the 4-probe resistance using a lock-in amplifier on both the heating and sensing sides. We haven't described the detailed error contributions for this term, but these are similar to those calculated in Shi [1]and Li [2] and as is seen later in this analysis, two orders of magnitude smaller in comparison to other sources of error in the measurement.

To determine the slope α_i, we use a temperature excursion of $\Delta T = 10K$. Then, $\delta(\Delta T_i) = \sqrt{2}\cdot\delta T_i \approx \sqrt{2}\cdot 40mK = 57mK$. Hence, $\frac{\delta(\Delta T_i)}{\Delta T_i} \approx \frac{57mK}{10K} \approx 5.7\times10^{-3}$. Therefore, we should expect $\left(\frac{\delta\alpha_i}{\alpha_i}\right) \approx 6\times10^{-3}$ at most from direct measurement of the 4-probe resistance and the cryostat temperature. However, this analysis doesn't account for temperature fluctuations of the cryostat ~30-40mK (at room temperature) which are unavoidable. We wait for up to 60 minutes at each gate temperature for the cryostat head temperature to stabilize. Hence, the maximum standard deviation of the estimated slope for either R_h or R_s is given by σ_α (obtained from the the least-squares linear fit to the Resistance, R_i vs

Temperature, T_i curve) where *i* represents either the heating or the sensing side. The equation that determines this value is:

$$\sigma_\alpha^2 = \sigma_R^2 \bullet \frac{n}{n\sum_i T_i^2 - \left(\sum_i T_i\right)^2}$$

where σ_R is the standard error for the Resistance estimate (either heating or sensing side) and *n* is the number of points taken (in this case, 5). σ_R is given by:

$$\sigma_R^2 = \frac{1}{n-2}\sum_i \left(R_i - \alpha T_i\right)^2$$

Then, in order to estimate the 95% confidence interval of the slope (considering two-tailed uniform distribution), we obtain a t-value of 3.182 for 3 *(n-2)* degrees of freedom. Thus, the maximum possible error in the slope is:

$$\delta\alpha_i = t_{(n-2)} \bullet \sigma_\alpha$$

which in terms of percentage can be written as (for beam I):

$$\frac{\delta\alpha_i}{\alpha_i} \le 0.76\%$$

Now, the error in ΔT_s and ΔT_h can be determined from the relation:

$$\frac{\delta(\Delta T_i)}{\Delta T_i} = \sqrt{\left(\frac{\delta(\Delta R_i)}{R_i}\right)^2 + \left(\frac{\delta\alpha_i}{\alpha_i}\right)^2} \approx \sqrt{\left(5\times10^{-5}\right)^2 + \left(0.76\times10^{-2}\right)^2} \approx 0.76\times10^{-2} = 0.76\%$$

Or as a general expression, $\frac{\delta(\Delta T_i)}{\Delta T_i} \approx \frac{\delta\alpha_i}{\alpha_i}$ where *i* stands for *h*(heating) or *s*(sensing).

Let us define $e_{\alpha_i} \equiv \frac{\delta\alpha_i}{\alpha_i}$.

Then, $\frac{\delta(\Delta T_i)}{\Delta T_i} \approx e_{\alpha_i}$

Now,

$$\frac{\delta(\Delta T_h + \Delta T_s)}{\Delta T_h + \Delta T_s} = \frac{\sqrt{[\delta(\Delta T_h)]^2 + [\delta(\Delta T_s)]^2}}{\Delta T_h + \Delta T_s} = \frac{\sqrt{(e_{\alpha_h}.\Delta T_h)^2 + (e_{\alpha_s}.\Delta T_s)^2}}{\Delta T_h + \Delta T_s}$$

Hence, from Equation (SI 5), neglecting the small error contributions due to terms $\frac{\delta I_h}{I_h}$ and $\frac{\delta R_h}{R_h}$, we can rewrite this equation as:

$$\left(\frac{\delta Q}{Q}\right)^2 \approx \left(\frac{\delta(\Delta T_s)}{\Delta T_s}\right)^2 + \left(\frac{\delta(\Delta T_h + \Delta T_s)}{\Delta T_h + \Delta T_s}\right)^2 \qquad \text{(SI 5a)}$$

which can be simplified with some simple algebra to determine the absolute error in the measured heat flux, δQ :

$$\delta Q = Q \bullet \sqrt{(e_{\alpha_s})^2 + \frac{(e_{\alpha_h}.\Delta T_h)^2 + (e_{\alpha_s}.\Delta T_s)^2}{(\Delta T_h + \Delta T_s)^2}} \qquad \text{(SI 7)}$$

We can thus estimate the error in Q(heat flux) for each ΔT (for beam I) to be:

$$\frac{\delta Q}{Q} = \sqrt{2 \cdot (4.2 \times 10^{-5})^2 + (5 \times 10^{-5})^2 + (0.76 \times 10^{-2})^2 + (1.2 \times 10^{-2})^2} \approx 1.4\%$$

Then, the error in conductance, G if defined as $Q/\Delta T$ is given by Equation (SI 6):

$$\frac{\delta G}{G} = \sqrt{(1.4 \times 10^{-2})^2 + (1.66 \times 10^{-2})^2} \approx 2.2\%$$

However, this is the error obtained for a single data-point for the case $G \equiv \frac{Q}{\Delta T}$. In practice, we obtain 200 such points during each measurement cycle as shown in Fig. S12 above. Further, we repeat each measurement cycle 2-3 times to ensure repeatability of

the data. Hence, a more accurate estimation of the beam conductance is given by the slope of the Q vs ΔT curve as the current, I_h, is ramped up. The difference is illustrated in the cartoon below:

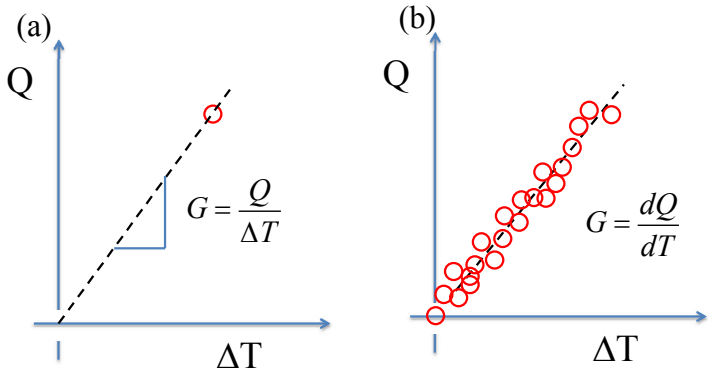

Fig. S13 Illustration of the difference in definition of the conductance either by considering (a) a single data-point with a large enough ΔT, or (b) taking the local slope of the heat flux for a variety of temperature gradients across the suspended beam.

To revisit the error bars in the case of Fig. S13(b), a similar analysis as described above can be performed. Since the slope of the Q vs ΔT curve (forcing the intercept to zero), gives the conductance, G, the standard error for the heat flux estimate as well as the error in conductance can be ascertained. As an example, data is reproduced below for beam I (see Table 1) in the manuscript:

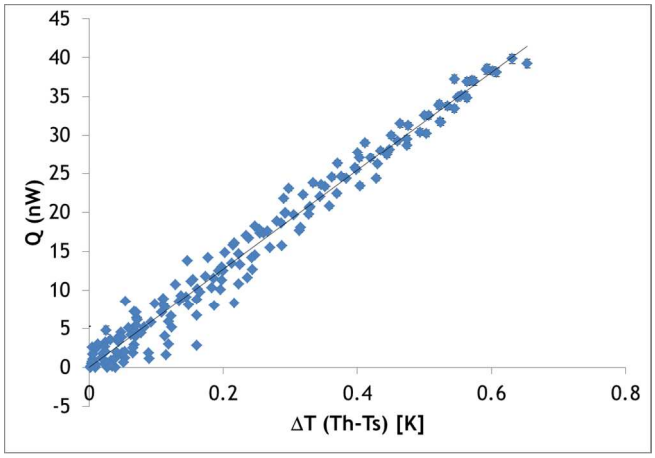

Fig S14 Heat flow through the tapered VO_2 beam I, Q in nW as a function of the temperature difference across the beam, ΔT in K at T_G = 300K.

Most importantly here, the error in heat flux is experimentally determined and can be called the pure error of each data point.

Hence, the conductance can be determined by doing a linear least-squared fit to the data. In our case however, weightage from the errors at small ΔT is overwhelming. Also, the variability in data for small ΔT is larger, thus the variance in the error is larger. As an example, consider the following residual plot in Fig S15(a), where the residual is defined as:

$$\varepsilon_i = Q_i - G_{fit}\Delta T$$

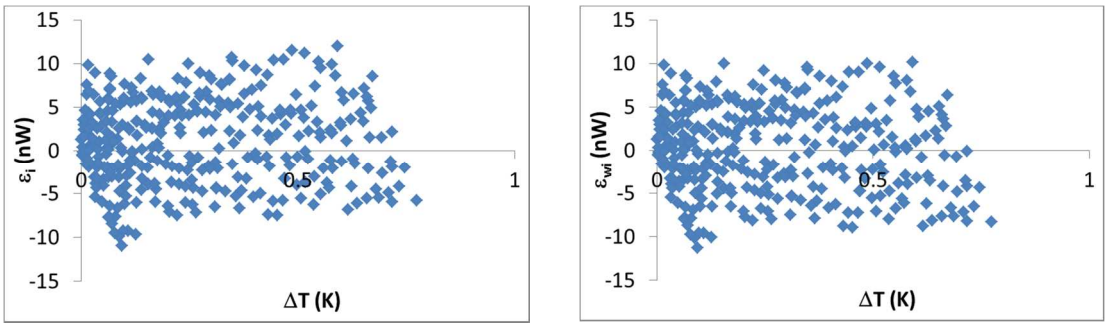

Fig S15(a) Residual plot for linear least-squared fit and (b) weighted linear least-squared fit, with a weight given by $w_i = 1/\delta Q^2$

Taking advantage of the large number of data points we gather at every global temperature, T_G we use the weighted least squares method to estimate the slope of the Q vs ΔT data. Similar to a simple linear least-squares regression, this will minimize the weighted residuals $s_w(G') = \sum_i w_i (Q_i - G'\Delta T_i)^2$, where $w_i = 1/\delta Q^2$

(see Fig S15b). This provides two advantages:

(1) it accounts for the non-equal error variance in the small ΔT case, and

(2) it incorporates the pure error, δQ in Q measurement at every ΔT in to the linear fit and hence accounts for actual experimental uncertainty.

It has been proven that such a weighted least-squares estimate is the best linear unbiased estimator (BLUE) when the weight is equal to the reciprocal of the measurement variance. Once the weighted least-squares fitting is completed, we can then estimate the error in conductance by considering the two-tailed 95% confidence interval with a $t_{(n-2)}$ value of 1.96 for n>100. Thus, the error in conductance is given by $\delta G = \sigma_G.(1.96)$.

In summary, for all beams measured, repeated measurements (2-3 times at each gate temperature) account for the error in Temperature Coefficient of Resistivity (TCR) of the Platinum Resistance Thermometers (PRTs), thus reducing the error in measured α_h and α_s. Secondly, slowly ramping up the heating current to get ~50-100 data points per temperature excursion allows for accurate estimation of the beam thermal conductance within 1% (depending on the cryostat temperature oscillations during measurement for each global gate temperature).

Finally, for our definition of error in rectification given by $R = \frac{G_+ - G_-}{G_-}$, we obtain for Beam I:

$$\frac{\delta R}{R} = \sqrt{\left(\frac{dG_+}{G_+}\right)^2 + \left(\frac{dG_-}{G_-}\right)^2} = \sqrt{\left(\frac{\delta G_+}{G_-}\right)^2 + \left(\frac{G_+}{G_-^2}\delta G_-\right)^2} \approx 1.3\% \qquad \text{(SI 8)}$$

where $G_+ \pm \delta G_+ = 80.1 \pm 0.6\,\text{nW/K}$ and $G_- \pm \delta G_- = 62.2 \pm 0.4\,\text{nW/K}$. A similar methodology is adopted to determine the error in thermal rectification for each of the VO_2 beams measured in the manuscript.

References

(1) Shi, L.; Li, D.; Yu, C.; Jang, W.; Kim, D.; Yao, Z.; Kim, P.; Majumdar, A. *J. Heat Transfer* **2003**, *125*, 881-888.

(2) Li, D. Thermal Transport in Individual Nanowires and Nanotubes, UC Berkeley, 2002.

(3) Keilmann, F.; Hillenbrand, R. *Philos. Trans. R. Soc. London A* **2004**, *362*, 787–805.

(4) Qazilbash, M. M.; Brehm, M.; Chae, B.-G.; Ho, P.-C.; Andreev, G. O.; Kim, B.-J.; Yun, S. J.; Balatsky, a V; Maple, M. B.; Keilmann, F.; Kim, H.-T.; Basov, D. N. *Science* **2007**, *318*, 1750–1753.

(5) Ocelic, N.; Huber, A.; Hillenbrand, R. *Appl. Phys. Lett.* **2006**, *89*, 1–3.

(6) Parker, J. *Phys. Rev. B* **1990**, *42*, 3164–3166.

(7) Kachi, S.; Kosuge, K.; Okinaka, H. *J. Solid State Chem.* **1973**, *6*, 258–270.

(8) Wells, A. F. *Structural Inorganic Chemistry*; Oxford Classic Texts in the Physical Sciences; OUP Oxford, 2012.

(9) Andreev, V. N.; Chudnovskii, F. A.; Petrov, A. V; Terukov, E. I. *Phys. Status Solidi* **1978**, *48*, K153–156.

(10) Berglund, C.; Guggenheim, H. *Phys. Rev.* **1969**, *185*, 1022–1033.

(11) Oh, D.-W.; Ko, C.; Ramanathan, S.; Cahill, D. G. *Appl. Phys. Lett.* **2010**, *96*, 151906.

(12) Yu, C.; Saha, S.; Zhou, J.; Shi, L.; Cassell, A. M.; Cruden, B. A.; Ngo, Q.; Li, J. *J. Heat Transfer* **2006**, *128*, 234-239.

(13) Incropera, F. P.; DeWitt, D. P. *Introduction to Heat Transfer*; Wiley, 2001.

(14) Utke, I.; Hoffmann, P.; Melngailis, J. *J. Vac. Sci. Technol. B Microelectron. Nanom. Struct.* **2008**, *26*, 1197-1276.

(15) Hadley, G. R. *Int. J. Heat Mass Transf.* **1986**, *29*, 909–920.

(16) Lyeo, H.-K.; Cahill, D. *Phys. Rev. B* **2006**, *73*, 1–6.

(17) Mavrokefalos, A.; Pettes, M. T.; Zhou, F.; Shi, L. *Rev. Sci. Instrum.* **2007**, *78*, 034901.

(18) Hochbaum, A. I.; Chen, R.; Delgado, R. D.; Liang, W.; Garnett, E. C.; Najarian, M.; Majumdar, A.; Yang, P. *Nature* **2008**, *451*, 163–167.

(19) Li, D.; Wu, Y.; Kim, P.; Shi, L.; Yang, P.; Majumdar, A. *Appl. Phys. Lett.* **2003**, *83*, 2934-2936.

(20) Dames, C. *J. Heat Transfer* **2009**, *131*, 061301.

(21) Majumdar, A.; Reddy, P. *Appl. Phys. Lett.* **2004**, *84*, 4768-4770.

(22) Tao, Z.; Han, T.-R. T.; Ruan, C.-Y. *Phys. Rev. B* **2013**, *87*, 235124.